

# THE SHAPE OF EXTREMELY METAL-POOR GALAXIES

Joseph Putko

Trabajo Fin de Máster

July 2018

Universidad de La Laguna

Master in Astrophysics

Supervisors: Jorge Sánchez Almeida & Casiana Muñoz-Tuñón

# Contents

|          |  |           |
|----------|--|-----------|
| <b>1</b> | <b>Resumen</b>   | <b>3</b>  |
| <b>2</b> | <b>Introduction</b>                                      | <b>7</b>  |
| 2.1      | What are XMPs, and why are they interesting?             | 7         |
| 2.2      | Scientific rationale for investigating shape of XMPs     | 9         |
| 2.3      | The axial ratio method for investigating intrinsic shape | 11        |
| 2.4      | Organization of this work                                | 14        |
| <b>3</b> | <b>Axial Ratio Measurement</b>                           | <b>14</b> |
| 3.1      | The Sample   | 14        |
| 3.2      | Using SExtractor   | 15        |
| <b>4</b> | <b>Results</b>   | <b>18</b> |
| 4.1      | Consistency checks on the axial ratio measurements       | 18        |
| 4.1.1    | Comparison with SDSS                                     | 18        |
| 4.1.2    | Comparison with different SExtractor input               | 21        |
| 4.2      | Evaluating potential bias due to seeing                  | 23        |
| 4.3      | Estimating error due to seeing                           | 27        |
| 4.4      | Evaluating potential surface brightness selection effect | 29        |
| 4.5      | Inferring thickness                                      | 30        |
| 4.6      | Inferring intrinsic shape                                | 32        |
| <b>5</b> | <b>Discussion</b>  | <b>35</b> |
| 5.1      | Why are XMPs thick?                                      | 35        |
| 5.2      | Why are XMPs triaxial?                                   | 36        |
| 5.3      | A brief comparison with other studies                    | 37        |
| 5.4      | The environment of XMPs                                  | 37        |
| <b>6</b> | <b>Conclusions</b>                                       | <b>38</b> |

|          |   |           |
|----------|---|-----------|
| <b>A</b> | <b>References</b>                                   | <b>40</b> |
| <b>B</b> | <b>Color images of omitted XMPs</b>                 | <b>42</b> |
| <b>C</b> | <b>Color images of XMPs in order of axial ratio</b> | <b>43</b> |
| <b>D</b> | <b>Additional figures</b>                           | <b>51</b> |

## 1 Resumen

Las galaxias extremadamente pobres en metales (XMPs) normalmente se definen como aquellas que tienen una metalicidad del gas ionizado inferior a una décima parte del valor de la metalicidad solar. Se cree que las galaxias XMPs deben de ser los tipos de galaxias más comunes en el Universo local, aunque generalmente no son detectadas a no ser que se encuentren en la fase “starburst.” Las galaxias XMPs starburst tienden a ser muy explosivas; la morfología típica es “cometaria” o “tadpole”, en la que el starburst es notablemente asimétrico y el componente subyacente (es decir, toda la galaxia salvo el starburst) es alargada. Solo hay unos cientos de galaxias XMPs con starburst, y la mayoría de ellas han sido descubiertas a partir del estudio del catálogo espectroscópico del Sloan Digital Sky Survey (SDSS).

Estas XMPs starburst tienen gran interés astrofísico. Primero, porque se han descubierto grandes inhomogeneidades en la distribución de su metalicidad. Como la escala de tiempos de la mezcla de gases en el disco de una galaxia es corta, el gas pobre en metales que desencadena el starburst tiene que haber sido acregado recientemente. Las simulaciones cosmológicas predicen que los discos de las galaxias son alimentados por la acreción de gas desde la red cósmica, y que este gas externo es quien mantiene la formación estelar en el tiempo. Este escenario de acreción de gas frío de origen cosmológico explicaría las caídas de metalicidad en las XMPs. Debido a que la formación estelar activa de las XMPs parece que es debida a la

incorporación de gas pobre en metales, las XMPs proporcionan una de las mejores evidencias observacionales disponibles de materia del medio intergaláctico sobre las galaxias en formación. En términos generales, las XMPs son de particular interés debido a que parecen ser galaxias de disco en sus etapas de formación tempranas, y son las mejores análogas en el Universo local de la primera generación de galaxias de baja masa. Por tanto, entender este tipo de galaxias puede ser de gran ayuda a la hora de comprender la formación y evolución de las galaxias.

El escenario de acreción de “cold-flow accretion” en cual el gas acretado directamente desde la red cósmica estimula la formación de galaxias de disco es una predicción robusta de los modelos cosmológicos aunque, desafortunadamente, cuenta con muy poca evidencia observacional. Como explicamos en el párrafo anterior, la caída de metalicidad en las regiones de formación estelar de las XMPs proporciona la mejor evidencia observacional disponible de las predicciones de los modelos, cosmológicos, pero es una evidencia primaria de la acreción de gas desde la red cósmica y no explica la estructura de las XMPs. La estructura de las XMPs no ha sido estudiada hasta el momento, aunque la galaxia subyacente tiene que ser una galaxia de disco para ajustarse las predicciones de los modelos. Hasta la fecha, en el único estudio que ha abordado la estructura de las XMPs de manera directa demostramos que estas galaxias tienen perfiles de luz exponenciales, como es de esperar en las galaxias de disco. El objetivo de este trabajo es caracterizar observacionalmente la forma tridimensional de la galaxias XMP a través de la medida del cociente entre los ejes mayor y menor medido en un conjunto grande de XMPs. Este enfoque revelará el grosor intrínseco de las galaxias y en qué grado son oblata, prolata o triaxial.

Se define la relación axial como el cociente entre la proyección del eje menor y la proyección del eje mayor. El método de la relación axial requiere medir la relación axial de un número estadísticamente significativo de galaxias, y posteriormente construir un histograma con la distribución de relaciones axiales observadas. Este histograma se puede modelar como una colección de elipsoides con orientación aleatoria con respecto al observador, cuyas propiedades se pueden inferir realizando

ajustes a la distribución observada. Un elipsoide oblató tiene dos ejes de igual longitud y un tercer eje más corto. A dicha morfología le corresponde una distribución de la relación axial plana y tendiendo a la unidad. El elipsoide prolato también tiene dos ejes de la misma longitud, pero el tercer eje es más largo que en el caso anterior. A dicha morfología le corresponde una distribución de la relación axial con un pico escarpado en el lado izquierdo del histograma (relación axial más baja). El elipsoide triaxial, por su parte, no tiene ningún eje de igual longitud, y su distribución de relación axial presenta dos picos. El grosor (relativo al eje mayor) se puede deducir a partir de la caída del histograma hacia pequeñas relaciones axiales, independientemente de la morfología intrínseca del objeto.

Las 196 fuentes de tipo XMP de Sánchez Almeida et al. (2016) fueron consideradas en este trabajo. Dicha muestra fue seleccionada para estudiar las propiedades de la clase XMP porque contiene la mayoría de las XMPs conocidas. Se realizaron mediciones sobre imágenes de SDSS de la banda r (data release 12). Se redujo el tamaño de la muestra a 171 galaxias tras inspeccionar visualmente las imágenes en banda r, conjuntamente con las imágenes a color SDSS g-r-i. Fueron omitidas las galaxias que parecían ser fusiones o satélites, y aquellos casos en que fuerzas de marea podrían estar presentes, debido a que en estos tres casos las galaxias probablemente sufren fuerzas externas que influyen en su forma. Para medir la relación axial, se utilizó el programa SExtractor ajustando una elipse a cada XMP y utilizando un umbral de fondo, para que pudiera ser considerada aquella señal más externa de las XMPs que se encontraba razonablemente por encima del ruido de fondo local. Cada elipse ajustada fue meticulosamente inspeccionada visualmente para asegurarnos de que el procedimiento funcionaba con exactitud, usando diagramas de contorno sobre versiones suavizadas de las imágenes como control.

El autor de este trabajo realizó comprobaciones en las medidas de relación axial variando el umbral de fondo utilizado para ajustar las elipses, repitiendo las medidas en la banda i de SDSS y comparando los resultados de SExtractor con las relaciones axiales medidas por las herramientas (pipelines) de reducción de SDSS.

Además, el error en las relaciones axiales se cuantificó teniendo en cuenta el seeing y tamaño de las galaxias. Sólo una de todas las medidas realizadas posee un error mayor de 0.12 en la relación axial, y el error medio es 0.02. Este pequeño error es un reflejo de que las XMPs son grandes en comparación con el seeing. El eje mayor medio de la muestra es 16.6 arcsec y el seeing medio es 1.2 arcsec.

La distribución de relación axial de la muestra de XMPs indica que las XMPs son morfológicamente gruesas, siendo las galaxias más pequeñas las más gruesas en proporción a su tamaño. Sólo el 8% de los XMPs tienen relaciones axiales inferiores a 0.4, pero estas galaxias son mucho mayores que la XMP estándar. No hay XMPs con menos de 5 kpc en su eje mayor que tengan una relación axial inferior a 0.4. La fuerte caída estadística en la distribución de la relación axial cerca de 0.4 sugiere que el espesor más común de XMPs es aproximadamente 0.4 veces el eje mayor. Por otro lado, hay una caída notable cerca de 0.5, y la existencia de múltiples caídas en la distribución de la relación axial observada es coherente con la idea de que el conjunto que las XMPs no comparte un espesor relativo único. Construí un modelo de galaxia para estimar el eje menor mínimo que puede ser medido, y el resultado de dicha simulación indica que las disminuciones en el histograma de relación axial a baja relación axial no son causadas por efecto del seeing.

La distribución de la relación axial también indica que las XMP son principalmente triaxiales y que un pequeño número pueden ser prolatas. La triaxialidad se infiere de la escasez de XMPs a alta relación axial, y de que el brillo superficial no disminuye con el aumento de la relación axial, ya que si la escasez fuese debida a un sesgo observacional el brillo superficial debería disminuir conforme aumenta la relación axial. Es importante destacar que la escasez de XMPs observadas a una alta relación axial no se debe a un efecto de selección en función del brillo superficial, ya que el 99% de las XMPs tienen brillo por encima del nivel de completitud espectroscópica del SDSS (90%).

La explicación más probable propuesta para la triaxialidad observada y el espesor de las XMPs es que son galaxias en proceso de formación, esto es, se cree

que la energía transportada por la caída de gas y la liberación de la energía cinética producida por la formación estelar producen un potencial gravitacional triaxial. Se cree también que ésta es una característica transitoria, porque las galaxias tienden a ser axi-simétricas cuando las fuerzas externas de ser importantes.

En el futuro queremos ajustar la distribución de la relación axial observada para cuantificar el grado de triaxialidad de la clase de galaxia XMP. Debido a que se observa que el grosor relativo varía con el tamaño de la galaxia y la distribución de la relación axial muestra múltiples caídas, la clase XMP debe ser separada en subconjuntos para que podamos hacer en el futuro un ajuste aún más preciso. Las medidas de la relación axial corregida por PSF, particularmente para las XMP más pequeñas, también facilitarían ajustar con mayor precisión la relación axial observada, haciendo posible cuantificar mejor el grado de triaxialidad de las XMPs.

## 2 Introduction

### 2.1 What are XMPs, and why are they interesting?

Extremely metal-poor galaxies (XMPs) are customarily defined to have an ionized gas-phase metallicity less than one tenth the solar value (e.g., Kunth & Ostlin 2000). As dwarf galaxies, XMPs have low mass and low luminosity. This is understood as metallicity and galaxy mass/luminosity share a positive correlation (e.g., Skillman et al. 1989). XMP galaxies are expected to be the most common type of galaxy in the local universe (e.g., Blanton et al. 2005; Sánchez Almeida et al. 2017), but they generally are not detected unless they are in a starburst phase. There are only a few hundred known starbursting XMPs, most of which have been discovered through mining the spectroscopic catalog of the Sloan Digital Sky Survey (SDSS; Morales-Luis et al. 2011; Izotov et al. 2012; Sánchez Almeida et al. 2016). XMPs tend to fit the characteristics of blue compact dwarf galaxies (BCDs; Morales-Luis

et al. 2011). XMPs and BCDs have a high blue surface brightness due to the presence of at least one ongoing starburst, but the underlying “host” component (i.e., all of the galaxy not including the starburst) contains aged stellar populations (e.g., Corbin et al. 2008) and is much fainter than the starburst (e.g., Caon et al. 2005). An example SDSS g-r-i color “mugshot” image of a typical XMP is shown in Figure 2.1, and mugshots of all of the XMPs studied in this work are shown in Appendices B and C.



**Figure 2.1:** An SDSS g-r-i “mugshot” image of J110552.92+602228.8 as an example of a typical XMP. Bright, blue, lopsided starbursts and faint, redder, elongated host components are very characteristic of XMPs. The image is 50 arcseconds across. The angular resolution is 1.5 arcsec, which corresponds to a spatial resolution of 0.14 kpc at the distance of the galaxy.

Most XMPs are highly irregular, and the most typical morphology is “cometary” or “tadpole” (Papaderos et al. 2008; Morales-Luis et al. 2011; Sánchez Almeida et al. 2016), in which the starburst is notably lopsided and the underlying host galaxy is elongated (see example in Figure 2.1). This galaxy morphology is extremely rare in the local universe, accounting for approximately 0.2% of the galaxies in the Kiso Ultraviolet Galaxy Catalogue (Elmegreen et al. 2012). While not all XMPs have



a textbook cometary morphology, the vast majority display some degree of asymmetry. Putko (2016) characterized only 3 out of 32 XMPs (the sample reported by Morales-Luis et al. 2011) as unambiguously symmetric (based on their smoothed contour plots), and indeed lopsidedness galaxies tend to have lower metallicity (Richard et al. 2009). In a random sample of cometary galaxies, there is a significant chance that some of them will be XMPs (Sánchez Almeida et al. 2013). This morphology-metallicity correlation may be due to the accretion of gas (Ceverino et al. 2012, 2016; Sánchez Almeida et al. 2013).

Large metallicity drops at the starbursts of the XMPs have been discovered (Sánchez Almeida et al. 2013, 2015). As the time-scale for gas mixing is short, the metal-poor gas triggering the starburst must have been accreted recently. Cosmological simulations predict that disk galaxies are fueled by the accretion of gas from the cosmic web and that this is the main driver of star-formation over cosmic time (e.g., Dekel et al. 2009).<sup>1</sup> This cold-flow accretion scenario would account for the metallicity drops at the starbursts of XMPs. Because the active star formation of XMPs seems to be due to accretion of metal-poor gas, XMPs are the best observational evidence for cold-flow accretion known to date.

## 2.2 Scientific rationale for investigating shape of XMPs

The cold-flow accretion scenario in which gas accreted directly from the cosmic web fuels the formation of disk galaxies is a prediction of cosmological models with minimal observational evidence (Sánchez Almeida et al. 2014). Evidence has been mounting in recent years with the discovery of large metallicity drops at the starbursts of XMPs (Sánchez Almeida et al. 2013, 2015), but this primary evidence does not address the structure of XMPs. The structure of XMPs has not been studied before, and we know that the underlying host component must be a disk galaxy to agree with model predictions. Characterizing the structure of XMPs will pro-

---

<sup>1</sup>I note that the same models that predict cold-flow accretion also predict galaxy-wide outflows driven by star-formation feedback.

vide a more complete picture of how they tie in to the cold-flow accretion scenario and may also offer implications for our understanding of cold-flow accretion and the stellar feedback processes that it triggers. More generally, XMPs are of significant astrophysical interest because, as they seem to be disk galaxies in early phases of formation, they are the best local analogs of the first generation of low-mass galaxies, and thus understanding them is fundamental to our broader understanding of galaxy formation and evolution.

Previous work (Putko 2016) used Sérsic’s model (Sérsic 1968) as a first step to characterize the shape of XMPs. A Sérsic profile models the brightness distribution of a galaxy or a component of a galaxy. Expressed as an intensity profile, Sérsic’s model is:

$$I(R) = I_e \exp \left\{ -b_n \left[ \left( \frac{R}{R_e} \right)^{\frac{1}{n}} - 1 \right] \right\}, \quad (2.1)$$

which has three free parameters in  $R_e$  (effective radius, which encloses half of the total light),  $I_e$  (intensity at the effective radius), and  $n$  (the “Sérsic index”). The constant  $b_n$  is defined in terms of  $n$  and ensures that  $R_e$  obeys its definition. The Sérsic index parameter is indicative of structure because the higher its value, the brighter and more centrally concentrated the light and the shallower the logarithmic slope at large radii. Giant elliptical galaxies and spheroidal components of disk galaxies are commonly modeled with  $n = 4$ , while  $n = 1$  (an exponential profile) is the canonical value for disks.

Using the Morales-Luis et al. (2011) sample of 32 XMPs, Putko (2016) found a median and mean Sérsic index of  $n \approx 1$  for the host components of the galaxies with  $0.5 \lesssim n \lesssim 2$  for the entire sample. This range is common for disk-like structure (e.g., Amorín et al. 2009). Thus, the light profiles of XMPs are consistent with the host components having a disk-like structure.

The aim of this current work is to uncover additional constraints on the three-dimensional shape of the XMP hosts by using another technique, introduced in the following section. Specifically, I will use the observed ratio between the minor and

major axes over a large sample of galaxies to infer properties describing the three-dimensional structure of XMPs. This approach will reveal the degree of intrinsic thickness of the galaxies, whether they are oblate or triaxial, and, if triaxial, the degree of triaxiality.

### 2.3 The axial ratio method for investigating intrinsic shape

Numerous studies have employed the axial ratio method to constrain the intrinsic shapes in large samples of galaxies (e.g., van den Bergh 1988; Binggeli & Popescu 1995; Sung et al. 1998a; Sung et al. 1998b; Elmegreen et al. 2005; Hunter & Elmegreen 2006; Ravindranath et al. 2006; Law et al. 2012; Roychowdhury et al. 2013), and this is the method I employ in this work. Axial ratio,  $q$ , is defined as the projected minor axis divided by the projected major axis.<sup>2</sup> The axial ratio method requires measuring axial ratio for a statistically significant number of galaxies and constructing a histogram of the measurements. This histogram represents a collection of randomly-oriented ellipsoids whose properties can be inferred through fitting. Figure 2.2 shows examples of theoretical axial ratio distributions for ellipsoids of three different intrinsic shapes oriented randomly to our line of sight. The oblate ellipsoid has two axes of the same length, and the third axis is shorter (e.g., a disk). The prolate ellipsoid also has two axes of the same length, and the third axis is longer (e.g., from a cigar to a rugby ball). The triaxial ellipsoid has no axes of equal length (e.g., a rugby ball that is compressed along its short axis). We see that only disks can show a distribution that is mostly flat and extending all the way to  $q = 1$ , and, from the cutoff at lower axial ratio, thickness is given by the minor axis regardless of intrinsic shape.

---

<sup>2</sup>Some studies use “ellipticity” ( $1 - \text{axial ratio}$ ) instead of axial ratio.

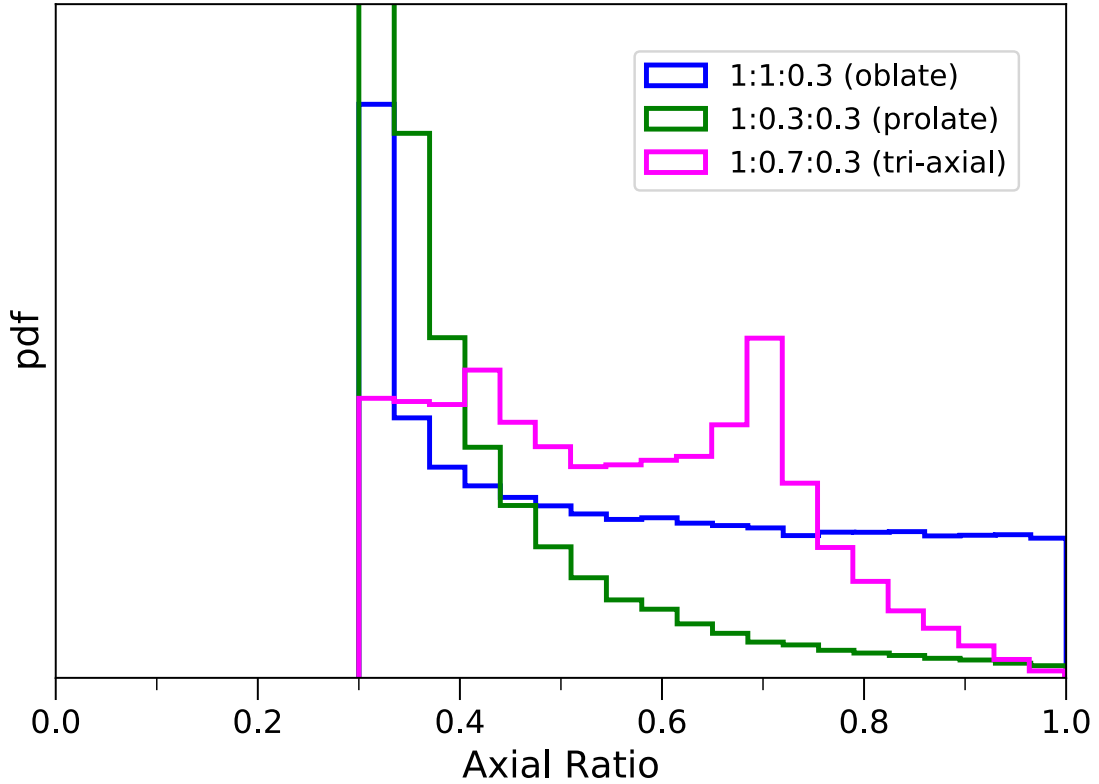


**Figure 2.2:** Theoretical axial ratio distributions for a collection of randomly-oriented oblate, prolate, and triaxial ellipsoids. The inset shows the color code used for each type of ellipsoid along with the corresponding ratio of axes. These ratios were constant in this simulation. The first green bin (more than twice as long as shown) is cropped to show more detail in the distributions.

The following explains how the distributions in Figure 2.2 were generated through a Monte Carlo simulation, and this will serve as the foundation for attempting to fit a theoretical axial ratio distribution to the observed axial ratio distribution for a large sample of XMPs (presented in Section 4.6). To obtain the models in Figure 2.2, each of the three distributions has been drawn from a sample of 20,000 galaxies. The axial ratio for each galaxy was derived using Equations (19) and (20) in Simonneau et al. (1998). They show that the semi-axes  $a$  and  $b$  of a projected ellipse from an ellipsoid with ratio of axes  $A:B:C$  can be determined from

$$a^2 b^2 = (A C \sin \beta \cos \alpha)^2 + (B C \sin \beta \sin \alpha)^2 + (A B \cos \beta)^2 = f \quad (2.2)$$

$$a^2 + b^2 = A^2 (\cos^2 \alpha + \cos^2 \beta \sin^2 \alpha) + B^2 (\sin^2 \alpha + \cos^2 \beta \cos^2 \alpha) + C^2 \sin^2 \beta = g, \quad (2.3)$$

for Euler angles  $\beta$  and  $\alpha$ , geometrically defined in Figure 2.3. For a random distribution of orientations, the angle  $\beta$  is drawn from a distribution where  $\cos \beta$  follows a uniform distribution between -1 and 1, and the angle  $\alpha$  follows a uniform distribution between zero and  $2\pi$  radians. As we see from Equations (2.2) and (2.3),  $a$  and  $b$  do not depend on  $\gamma$ , the third Euler angle. Using Equations (2.2) and (2.3), the axial ratio is given by

$$q = \frac{1 - h}{1 + h}, \quad (2.4)$$

where

$$h = \sqrt{\frac{g - 2\sqrt{f}}{g + 2\sqrt{f}}}. \quad (2.5)$$

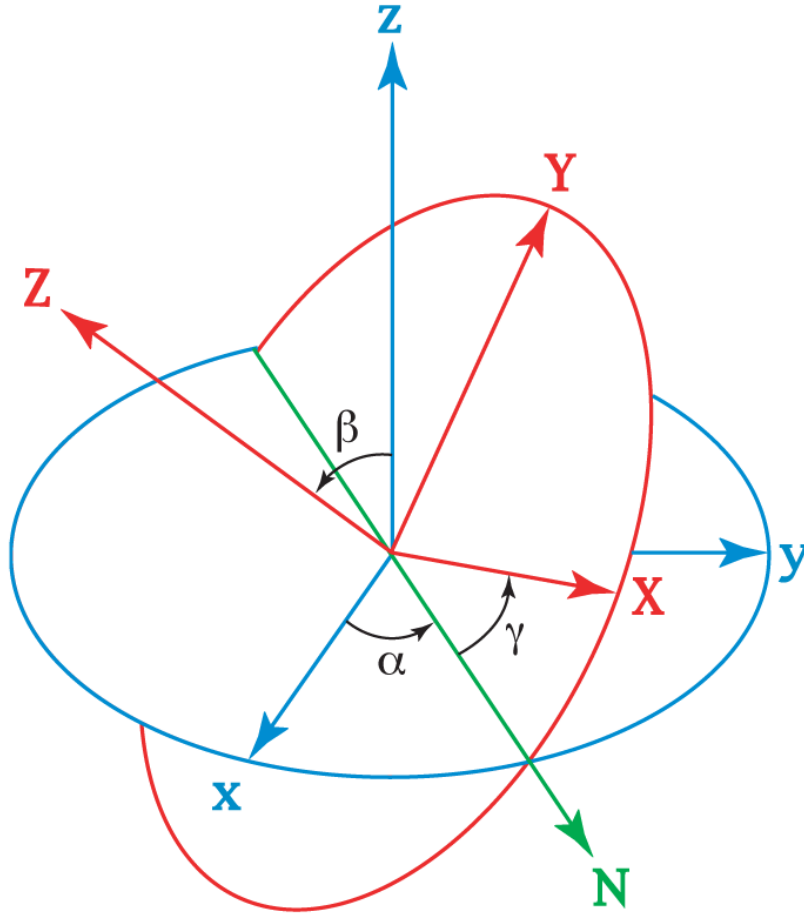


**Figure 2.3:** Geometric definition of Euler angles  $\alpha$ ,  $\beta$ , and  $\gamma$ . The fixed system  $xyz$  is in blue, the rotated system  $XYZ$  is in red, and the green line defines the line of nodes. Image from the free media repository Wikimedia Commons.

## 2.4 Organization of this work

Section 3 of this work explains how the XMP sample used for the measurements was refined and the steps taken for measuring axial ratio. Section 4 includes numerous checks on the measurements, including evaluation of uncertainty, biases, and error; a preliminary theoretical axial ratio distribution is offered for comparison with the observed XMP axial ratio distribution; and inferences regarding intrinsic shape are presented. Section 5 discusses the results, including an exploration of the possible explanations for the inferred constraints on intrinsic shape, and Section 6 summarizes the findings of this work.

# 3 Axial Ratio Measurement

## 3.1 The Sample

The sample of 196 XMP sources from Sánchez Almeida et al. (2016) was considered in this work. It is used to study the properties of the XMP class in general because it contains the majority of the known XMPs. Measurements were made on the r-band SDSS images of data release 12 (Alam et al. 2015). The r band was used because it has the highest signal-to-noise ratio for the host component of the galaxies. The sample size was reduced to 171 galaxies after visually inspecting the r-band fits images in conjunction with SDSS g-r-i color images. Galaxies were omitted if they appeared to be mergers or satellites or if tidal features were present because such galaxies are likely to have external forces influencing their shape. Other XMPs were omitted simply due to the presence of a prominent overlapping source. In the case of I Zwicky 18, its two clumps registered as separate XMPs, so one of them was omitted. Lastly, two sources were omitted on account of unsuccessful deblending (see Section 3.2). Table 3.1 lists which sources were omitted and the reason for omission, and their SDSS color images are shown in Appendix B.

**Table 3.1:** Omitted XMP Sources

| XMP <sup>a</sup> | Reason for Omission             |
|------------------|---------------------------------|
| 3                | tidal tail                      |
| 9                | contamination                   |
| 20               | HII region / merger / satellite |
| 44               | duplicate of 43                 |
| 49               | merger?                         |
| 55               | contamination / merger?         |
| 60               | contamination                   |
| 85               | merger?                         |
| 93               | merger?                         |
| 98               | merger?                         |
| 111              | contamination?, tidal tail      |
| 130              | merger?                         |
| 136              | merger?                         |
| 138              | merger?                         |
| 140              | merger?                         |
| 142              | merger?                         |
| 147              | merger?                         |
| 154              | contamination?                  |
| 158              | unsuccessful deblending         |
| 171              | merger?                         |
| 178              | unsuccessful deblending         |
| 186              | merger?                         |
| 187              | merger?                         |
| 193              | tidal tail                      |
| 194              | merger?                         |

<sup>a</sup>XMP index number according to Sánchez Almeida et al. (2016).

### 3.2 Using SExtractor

To measure the projected shape the galaxies, SExtractor (*Source-Extractor*; Bertin & Arnouts 1996) was used to fit an ellipse to each XMP. SExtractor uses the flux-weighted second-order moments of the objects to generate the fit. I used a detection threshold of  $1.5\sigma$ , meaning SExtractor considered pixels 1.5 times above the local background's standard deviation as part of an object. This forced the measurement to consider the outermost light of the XMP host that is reasonably above the local background noise.

Each fitted ellipse was meticulously visually inspected for accuracy. To judge

if a fit looked reasonable, I compared it to the outermost well-defined contours on a smoothed version of the image. (SExtractor measured the galaxies without smoothing applied, as smoothing would tend to make the objects rounder, i.e., give higher axial ratio.) An example is shown in Figure 3.1 considering XMP 178; no combination of SExtractor deblending settings could extract the entire XMP as a single source. Note that the ellipse fitted to the XMP is not consistent with the outermost contours in the contour plot.

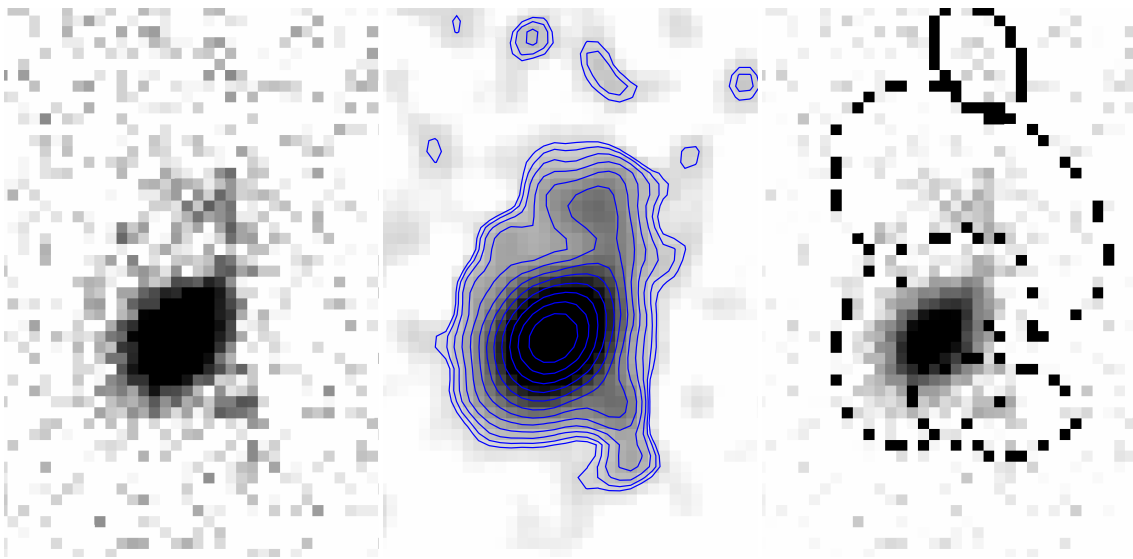


**Figure 3.1:** An example of SExtractor failing to provide an accurate fit. At left is the original SDSS r-band image of XMP 178; in the center panel logarithmic contours are applied to a smoothed version of the image; and at right is the SExtractor check image showing the fitted ellipse. The ellipse around the brightest portion of the object is clearly inconsistent with the outermost contours in the center panel, as proper deblending could not be achieved. Contour plots were used as shown in this example for each XMP measured to identify clearly inaccurate ellipse fits.

Experimenting with the deblending settings was also necessary for XMPs with multiple clumps. An example is shown in Figure 3.2, showing improper deblending versus proper deblending for an XMP with two prominent clumps. Finally, checking each fitted ellipse required careful attention to nearby or overlapping objects. It was not always immediately clear what was part of the galaxy and what was not, but inspecting the SDSS color images along with the contour plots on the smoothed fits images allowed for making decisions with a reasonable degree of confidence. Figure



3.3 shows an example in which an overlapping source was successfully extracted and thus not contributing to the ellipse fitted to the XMP. In measuring an object's flux when a source is overlapping, SExtractor corrected for this by assuming the object is symmetrical with respect to the object's center.

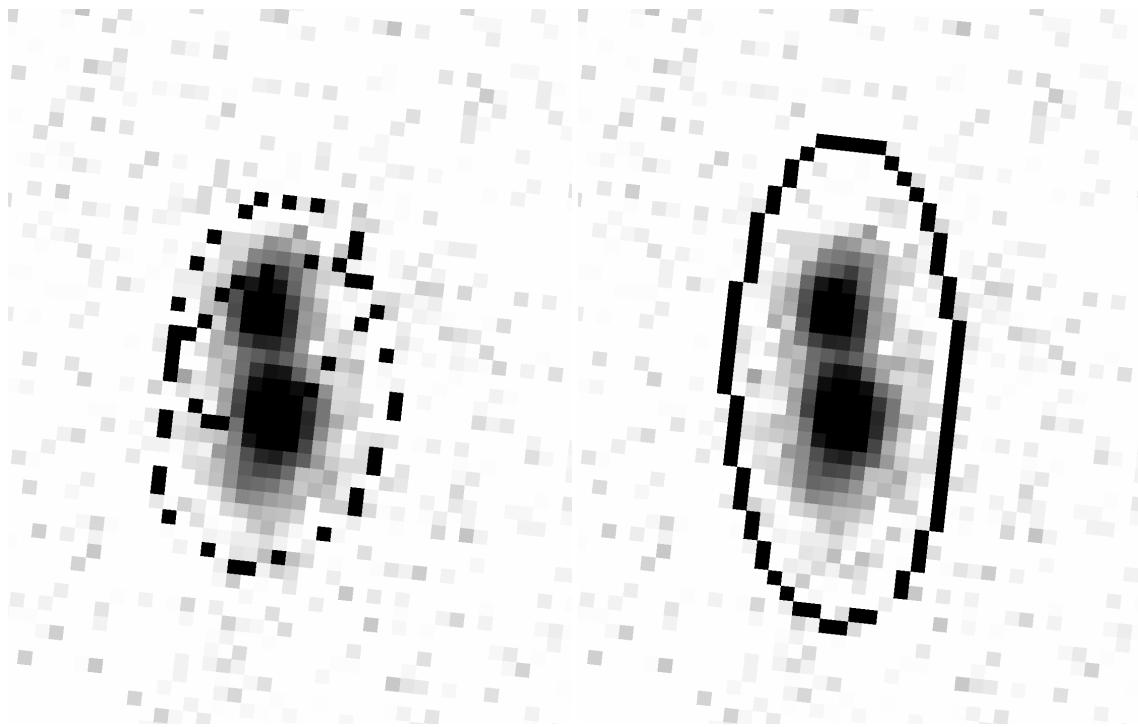


**Figure 3.2:** Two different SExtractor “check images” (fits files showing the fitted ellipses to the sources extracted) of XMP 190. The galaxy has two massive clumps, requiring the deblending settings within SExtractor to be adjusted as appropriate. The dashed ellipses at left are SExtractor’s way of suggesting highly uncertain fits.

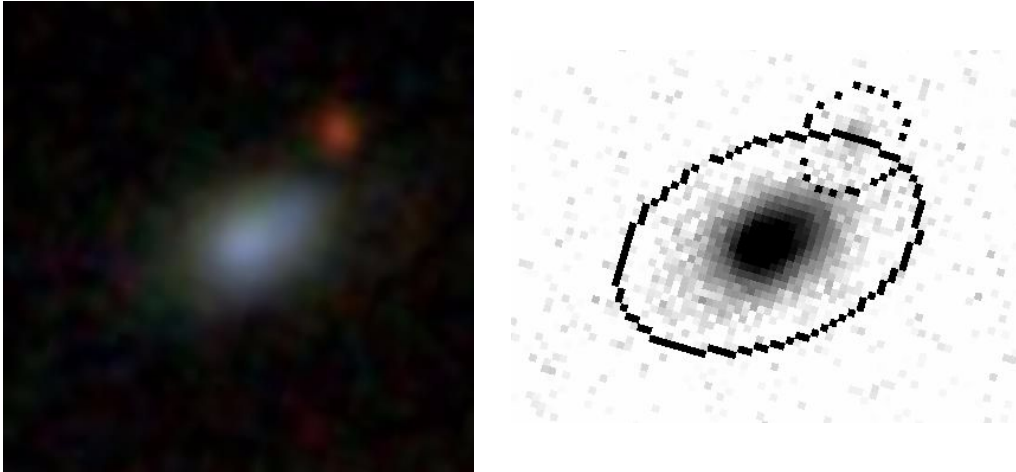


**Figure 3.3:** SDSS mugshot of XMP 176 (left) and the resulting SExtractor check image (right) showing the fitted ellipses to the XMP and the overlapping background source. Each ellipse fitting attempt made sure that any sources overlapping with the XMP were extracted as separate objects.

## 4 Results

### 4.1 Consistency checks on the axial ratio measurements

#### 4.1.1 Comparison with SDSS

The previous section highlighted how the process of fitting the ellipses was carried out with extreme care, but I still performed a number of consistency checks on the SExtractor axial ratio measurements ( $q = b/a$ , in the notation of Section 2.2). Axial ratio is measured by the SDSS reduction pipelines, and while these measurements obtained in an automated fashion should not be used blindly because of the issues highlighted in Sections 3.1 and 3.2, strong agreement between the SDSS axial ratios and my SExtractor measurements would give weight to the reliability of my measurements.

The SDSS provides three different measures for axial ratio. The first is known as  $q_{\text{Stokes}}$ , which, similar to SExtractor’s method, is also found from the flux-weighted second-order moments of an object. However, as demonstrated in Alam & Ryden (2002), SDSS allows the measurement to be dominated by the innermost isophotes, whereas I forced SExtractor to consider the outermost light. Therefore,  $q_{\text{Stokes}}$  is not a useful measure to describe the apparent shapes of the XMP hosts.

Of the other two measures of axial ratio provided by SDSS, one is based on fitting an exponential profile to the galaxy, and the other is based on a de Vaucouleurs profile, and these measures are dominated by the outer region of a galaxy (Alam & Ryden 2002). Unlike  $q_{\text{Stokes}}$ , these measures take into account the PSF to correct for seeing effects. Because XMPs have exponential profiles (Putko 2016), I compare my SExtractor axial ratios to the SDSS ones based on exponential fitting, as shown in Figure 4.1.<sup>3</sup> More than half (91 of 171) of the SExtractor measurements are within  $\pm 0.1$  the SDSS value for axial ratio, suggesting a significant degree of agreement between the two values, but significant outliers, such as XMPs 139 and 157, highlight that the SDSS measurements should not be used blindly. In these two extreme cases, SDSS clearly mistook a feature of the galaxy for the whole galaxy, whereas my SExtractor measurements ensured that the entire galaxy was properly detected. Out of the 91 cases where the SExtractor axial ratio is within  $\pm 0.1$  the SDSS value, in 61 of them, the SExtractor measurement is greater than the SDSS value. This bias could be due to that SDSS is correcting for seeing.

---

<sup>3</sup>The axial ratios based on exponential profile fitting by SDSS are compared to  $q_{\text{Stokes}}$  in Figure D.1.

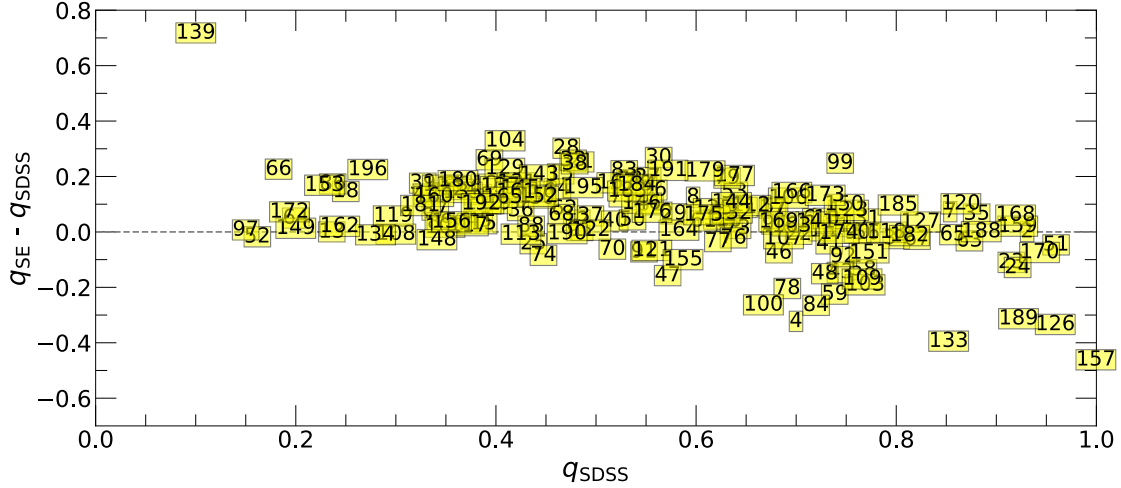


**Figure 4.1:** Comparing XMP axial ratios as measured by SExtractor (SE) in this work versus measurements by the SDSS. The SDSS provides three different measures for axial ratio, and the one based on an exponential profile fit is used here. The numbered markers correspond to XMP index number according to Sánchez Almeida et al. (2016).

This issue that the SDSS measurements should not be used blindly is further highlighted in Figure 4.2, which compares the difference in total galaxy flux in terms of apparent magnitude with the difference in measured axial ratio between SExtractor and SDSS. We see several points reflecting SDSS measured a smaller flux and that the largest differences in magnitude correspond to the largest differences in measured axial ratio. Clearly, SDSS occasionally strongly misses identifying the whole galaxy.

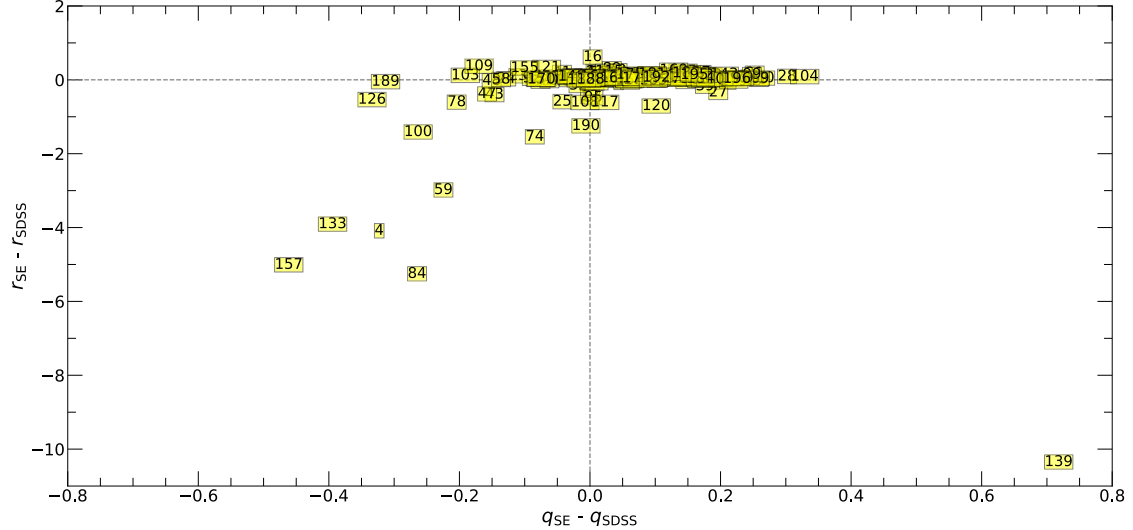


**Figure 4.2:** The difference in r-band magnitude versus the difference in axial ratio, comparing measurements made by SExtractor (SE) with those by the SDSS. It is never the case that SExtractor measures a significantly lower flux, but in several cases SDSS measures a much lower flux, and these cases occur when a significant difference in axial ratio is also observed. Clearly, SDSS sometimes did not properly detect the entire galaxy. For this reason, the SDSS axial ratio measurements are not reliable on their own for studying XMPs. The numbered markers correspond to XMP index number according to Sánchez Almeida et al. (2016).

#### 4.1.2 Comparison with different SExtractor input

Further checks were carried out by considering a different background threshold and a different filter on a subset of the sample. The i band was considered using the same  $1.5\sigma$  background threshold, and the difference in axial ratios are shown in Figure 4.3. The vast majority of cases show a difference smaller than 0.1, the scatter above and below zero appears symmetric, and higher axial ratios appear to have higher uncertainty. Figure 4.4 reflects how the results change when using a  $2.5\sigma$  background threshold. We see a tighter scatter compared to that in Figure 4.3, with the vast majority of cases now showing a difference smaller than 0.05, and again higher axial ratios appear to be more uncertain. Figures 4.3 and 4.4 help qualify the uncertainty in the axial ratio measurements in addition to serving as useful consistency checks.

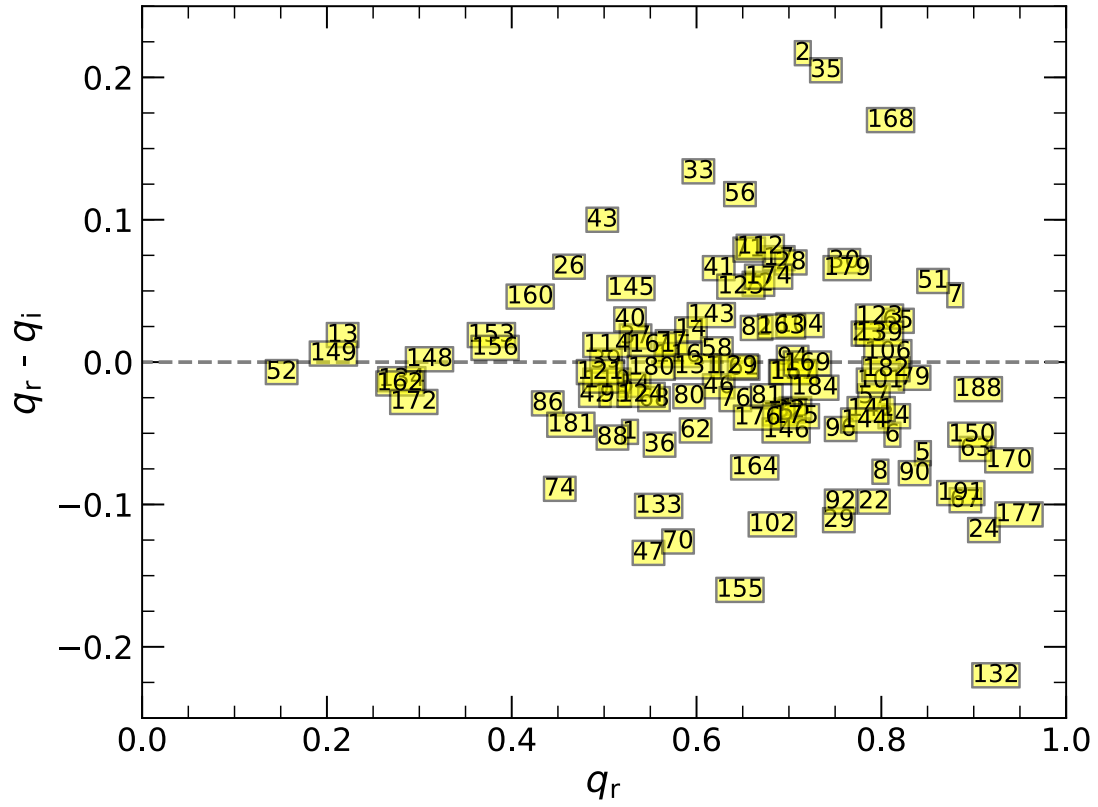


**Figure 4.3:** Comparison of axial ratios measured by SExtractor in the r band versus the i band under identical SExtractor settings. The numbered markers correspond to XMP index number according to Sánchez Almeida et al. (2016).

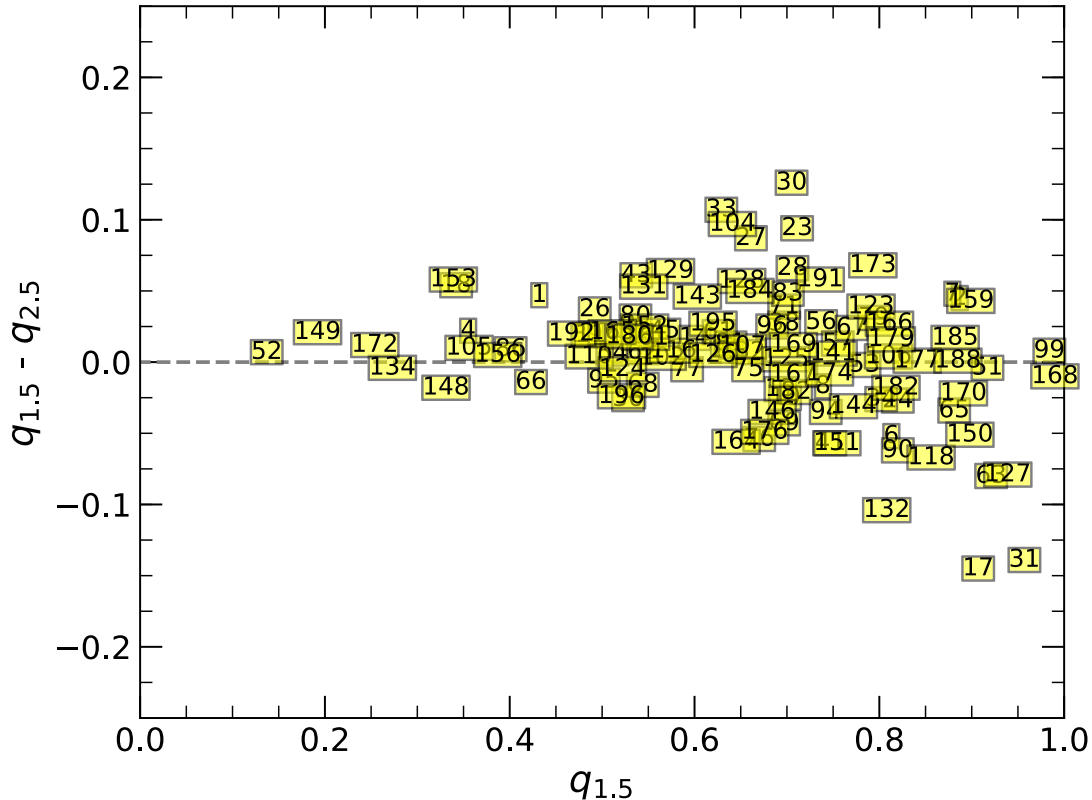


**Figure 4.4:** Comparison of axial ratios measured by SExtractor in the r band using a  $1.5\sigma$  background threshold versus a  $2.5\sigma$  threshold. The numbered markers correspond to XMP index number according to Sánchez Almeida et al. (2016).

## 4.2 Evaluating potential bias due to seeing

It is necessary to evaluate if seeing is responsible for cutting off the axial ratio distribution at lower axial ratio values. The distribution of the measured axial ratios is shown in Figure 4.5 along with an estimation of what the distribution would look if all of the galaxies were edge-on and as thin as seeing would allow to be observed, which I refer to as the “seeing-limited” distribution. Figure 4.6 highlights how the minimum measurable minor axis was derived. I began with a model galaxy one pixel thick and convolved this with a circular Gaussian function for a seeing of 1.2 arcsec, the median seeing of the sample (the seeing distribution of the sample is shown in Figure D.2). The result was added to an empty section of background in one of the r-band images in the data set. An ellipse was then fitted using SExtractor, and the

resulting minor axis is 3.5 arcsec (for different initial major axes, this result varies by less than one tenth of a pixel). The background noise is largely uniform among the sample, so, instead of convolving the model galaxy with each seeing value in the data set, I assumed the ratio of the hypothetical minimum minor axis to the seeing is constant. Thus, for each galaxy:

$$\textit{hypothetical minimum minor axis} = \frac{3.5}{1.2} \times \textit{seeing} . \quad (4.1)$$

This value was then divided by the observed major axis for each galaxy to obtain the seeing-limited axial ratio. In Figure 4.5 we see the vast majority of the seeing-limited axial ratios are to the left of the major fall-off in the observed distribution near axial ratio 0.4. This demonstrates that seeing is not responsible for the fall-off in observed axial ratio.



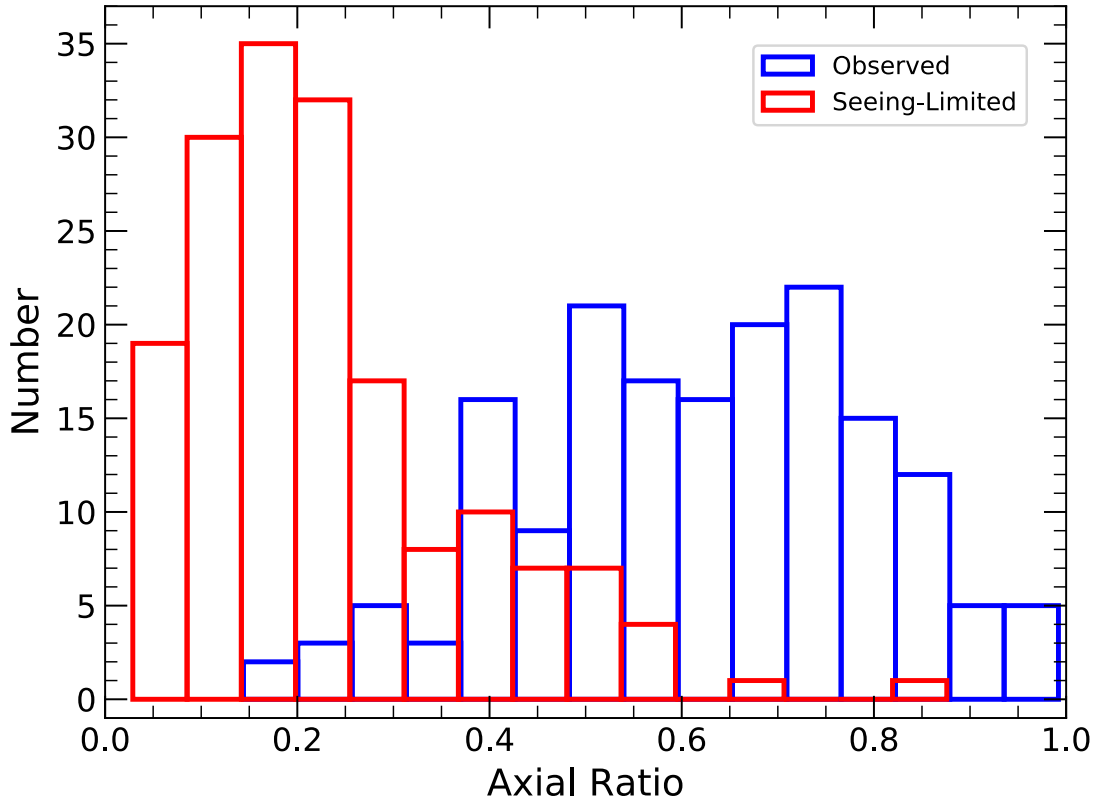


**Figure 4.5:** Distribution of the observed axial ratios for 171 XMPs, and a hypothetical “seeing-limited” axial ratio distribution. The hypothetical distribution was constructed using the observed major axes and assuming all of the galaxies are edge-on, 1 pixel thick, and observed under seeing conditions corresponding to the PSF value provided by SDSS for each r-band frame. The bulk of the seeing-limited distribution falls to the left of the bulk of the observed distribution, suggesting the fall-offs in the observed distribution are not caused by seeing.

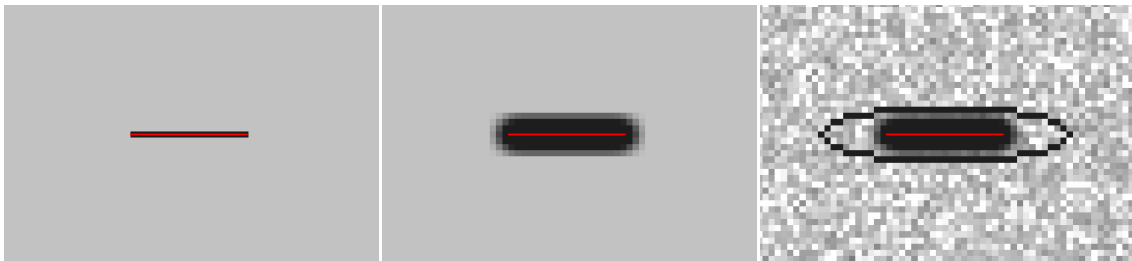


**Figure 4.6:** A simulation to estimate the minimum minor axis that SExtractor can measure considering seeing. A model edge-on galaxy initially 1 pixel (0.4 arcsec) thick (left panel) was convolved with a circular Gaussian function (center panel) considering 1.2 arcsec seeing and added to an empty background section of a real image (right panel). The final image was measured with SExtractor to produce the fit shown, giving a minor axis of 3.5 arcsec. For reference, the red line is the same size and in the same position in all of the panels.

There is also a notable fall-off near axial ratio 0.5 in Figure 4.5, and there are 10 XMPs with seeing-limited axial ratios greater than 0.5. The smallest galaxies will be more affected by seeing, and smaller XMPs do tend to be rounder, as shown in Figure 4.7, which plots minor versus major axis with axial ratio reference lines overlaid. All of the points in Figure 4.7 fall above the median minimum measurable minor axis of 3.5 arcsec, but some of the points have a minor axis very close to this value. To assess whether any individual axial ratio measurement is entirely uncertain due to seeing, Figure 4.8 plots observed axial ratio minus the estimated seeing-limited axial ratio for each galaxy. None of the points reach zero, when observed axial ratio would equal seeing-limited axial ratio, and the vast majority of cases show a difference greater than 0.2.

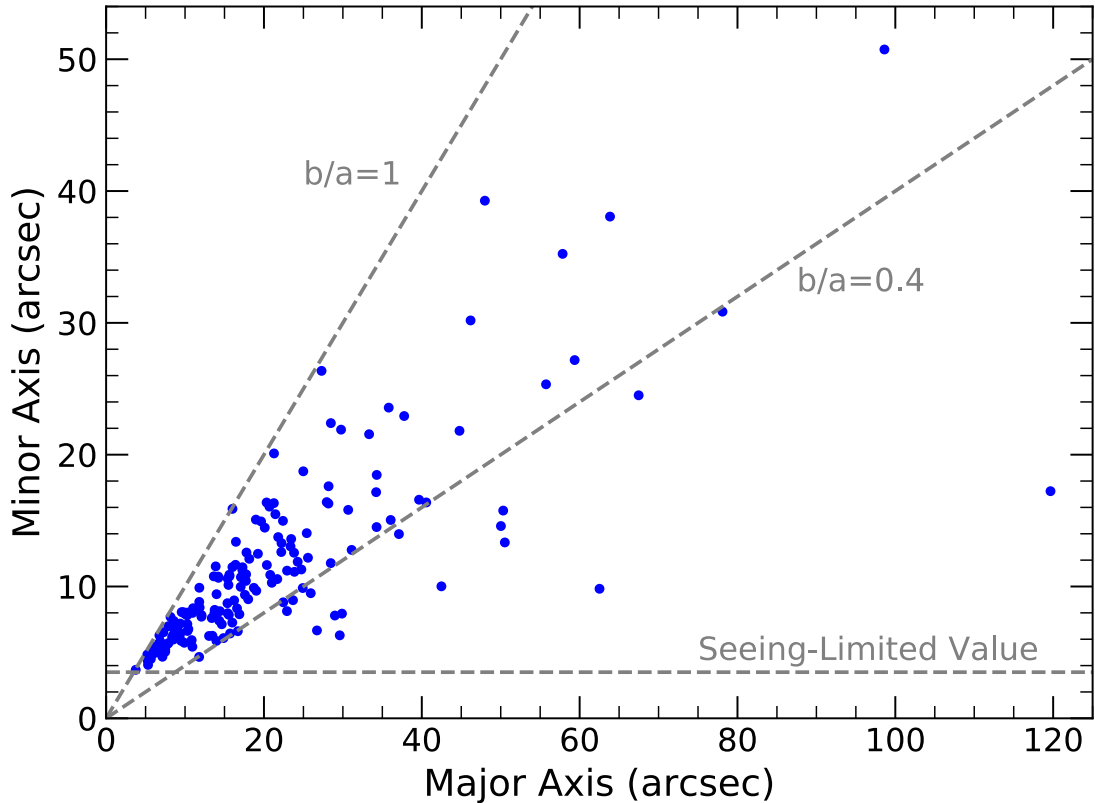


**Figure 4.7:** Minor axis versus major axis of the ellipses fit to the XMPs using SExtractor. The horizontal line at 3.5 arcsec indicates the minimum observable minor axis that 1.2-arcsec seeing allows, which is the median seeing for the sample. For reference, a diagonal line is shown for two different axial ratio values.

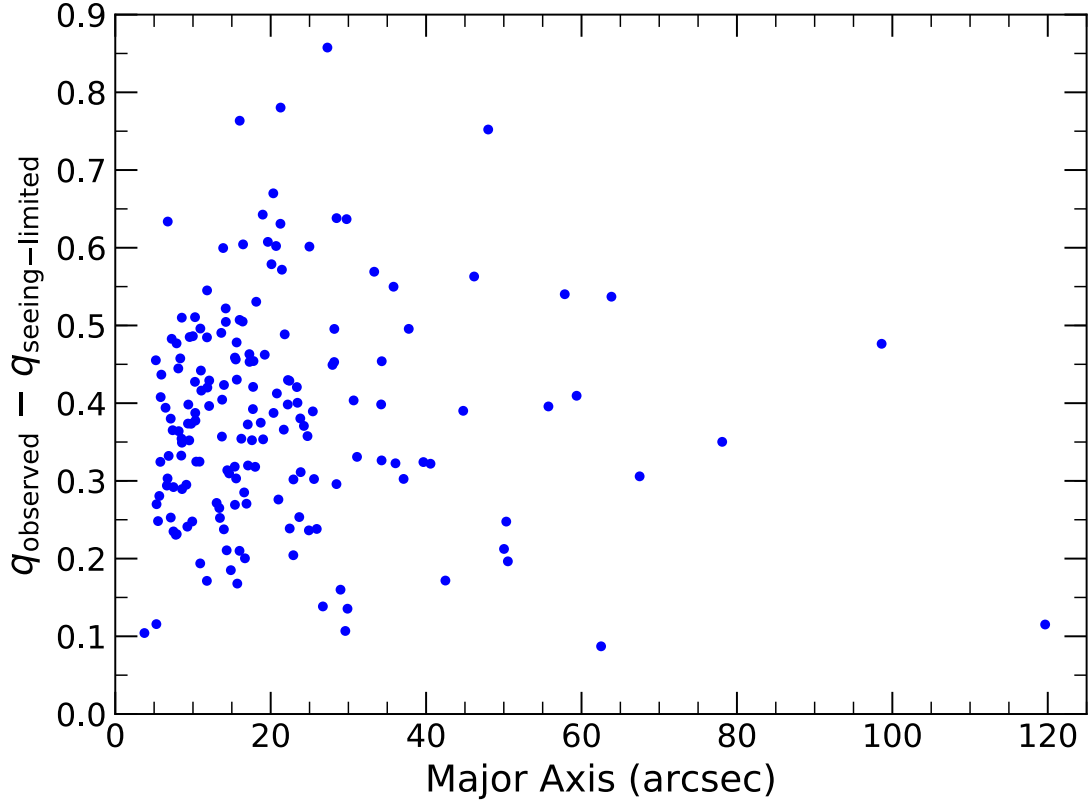


**Figure 4.8:** The difference between observed axial ratio and the estimated seeing-limited axial ratio (the minimum measurable axial ratio that seeing would allow) shown against galaxy angular size. None of the observed axial ratios are entirely uncertain, as none of them are equal to their corresponding seeing-limited axial ratio.

Figure 4.8 suggests the observed axial ratio distribution is not strongly affected by seeing, but we see in Figure 4.7 that a galaxy must be greater than 8.75 arcsec (assuming 1.2-arcsec seeing) in major axis before it is possible to measure an axial ratio smaller than 0.4. The SExtractor axial ratio measurements may be affected by seeing in a non-negligible way for the smallest XMPs in angular size, and the following section explores the magnitude of this error.

### 4.3 Estimating error due to seeing

To quantify the error in the axial ratio measurements due to seeing, I consider the approximation  $a_o^2 = a^2 + s^2$  and  $b_o^2 = b^2 + s^2$ , which relates the observed major

( $a_o$ ) and minor ( $b_o$ ) axes and the true major ( $a$ ) and minor ( $b$ ) axes for a seeing  $s$ . Using these expressions, one can derive

$$q_o - q \equiv q_o \left( 1 - \sqrt{\frac{1 - (s/b_o)^2}{1 - (s/a_o)^2}} \right) = \text{axial ratio error} \quad (4.2)$$

to represent the axial ratio error due to seeing. The estimated axial ratio errors are shown in Figure 4.9. As expected, the error tends to be larger for smaller galaxies; however, even for these cases the error is not terribly large. In only one case is the error greater than 0.12. The median error is 0.02. The error inflicted by seeing is small because the galaxies are large in comparison to the seeing. It thus appears that the main reason smaller XMPs tend to be rounder is because they are thicker in comparison to their major axis (see Section 4.5).

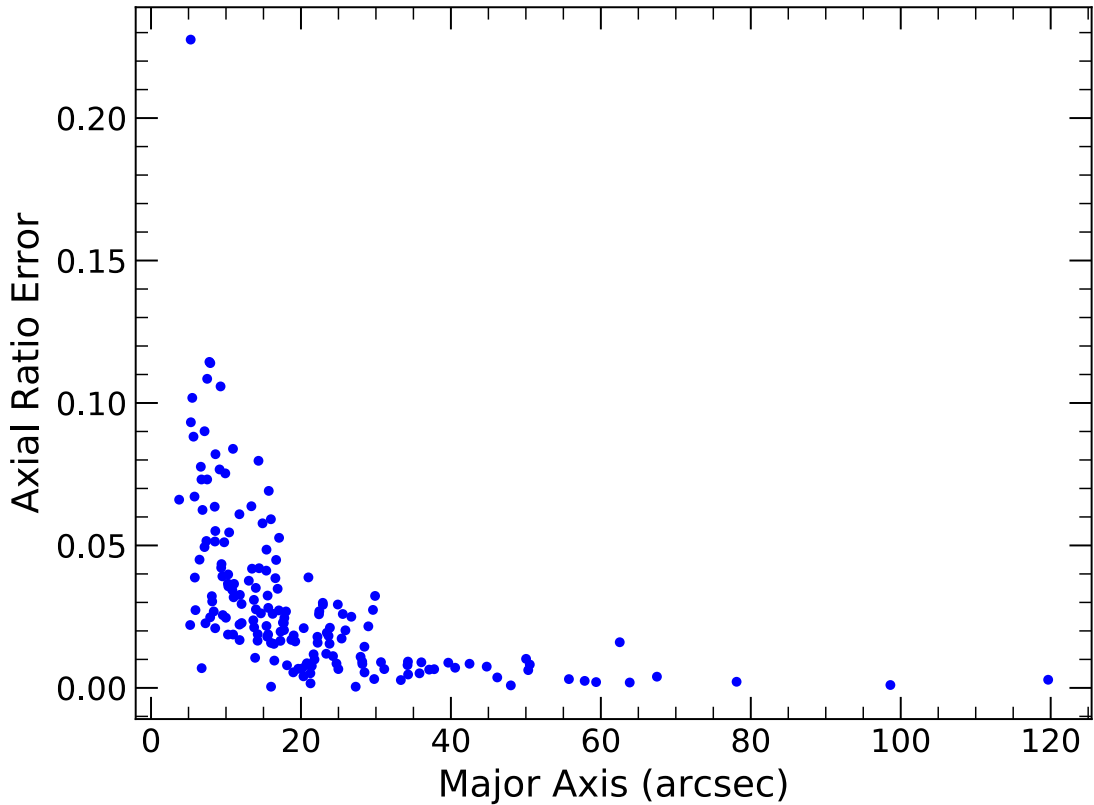


**Figure 4.9:** Estimated axial ratio error (using Equation 4.2) caused by seeing versus major axis for the XMPs. The SDSS reported PSF value for each image was used for the seeing.

## 4.4 Evaluating potential surface brightness selection effect

It is expected that inclined disks would be over-represented compared to face-on galaxies near the surface brightness limit of a survey (e.g., Elmegreen et al. 2005) because the integration along the line of sight in edge-on disks gives a higher surface brightness, and surveys are biased against low surface brightness objects (e.g., Blanton et al. 2005). To test if there is a bias against face-on XMPs, I calculated the half-light surface brightness, or the mean surface brightness within the effective radius, for the sample using the SExtractor measurements for magnitude and effective radius. These values are shown in Figure 4.10 along with the 90% spectroscopic completeness level of SDSS (taken from Figure 3 in Blanton et al. 2005). Only two measurements fall below this level. Moreover, we do not see surface brightness decline with increasing axial ratio. Thus, it appears conclusive that this study is not meaningfully biased by a surface brightness limit.

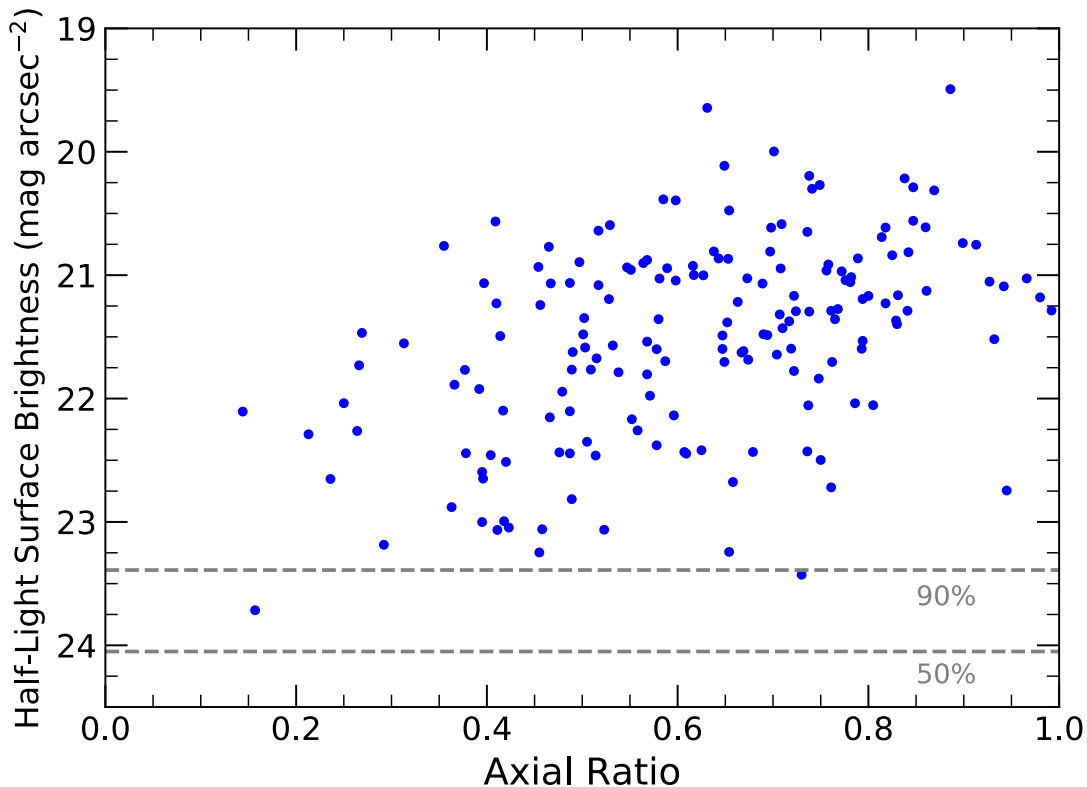


**Figure 4.10:** Half-light surface brightness versus axial ratio for the XMPs. The dashed lines indicate the SDSS spectroscopic completeness levels (from Figure 3 in Blanton et al. 2005). Only two of the measurements are below the 90% completeness level, indicating there is not a meaningful surface brightness selection effect against the XMPs.

It was noted in the previous section that there is a bias toward higher axial ratio due to seeing. Even with this bias, we still observe a significant dearth of XMPs near 1 in axial ratio. In Figure 4.7, we see there are only three XMPs with axial ratio near 1 that are well beyond the region of smallest XMPs, whose measurements are more susceptible to error due to seeing.

## 4.5 Inferring thickness

Figure 4.8 shows that observed axial ratio is within  $\sim 0.1$  of seeing-limited axial ratio in extremely few cases. Therefore, the XMPs have a thickness that we can measure. The thickness of the XMPs relative to their size can be quantified

and inferred from the fall-off in the axial ratio distribution at lower axial ratios. In Figure 4.5 we observe a significant fall-off near axial ratio 0.4. This suggests that the average thickness of the XMPs is  $\sim 0.4$  times the major axis. There are only 10 XMPs with a measured axial ratio smaller than 0.35. Appendix C shows the SDSS color images of the galaxies in order of increasing axial ratio, and these 10 XMPs are all of the ones through XMP 148. Among the first 10 in the list in Appendix C, XMPs 52, 149, and 134 do not look like typical XMPs given their redder appearance and no obvious starbursts.

Another way to note the dearth of XMPs with an axial ratio smaller than 0.4 is in Figure 4.7, as there are very few XMPs beyond the 0.4 axial ratio reference line. Figure 4.7 also shows that the first XMP with an axial ratio smaller than 0.4 is 22 arcsec in major axis. Thus, it appears that the smaller an XMP is, the thicker it tends to be relative to its size. This is supported in Figure 4.5 as there is also a notable fall-off in axial ratio near 0.5. This suggests some of the XMPs are very thick for their size, with some having a thickness half the size of the major axis. The cut-off near 0.2 and the fall-offs near 0.4 and 0.5 strongly evidence that the XMPs do not share a common relative thickness and that the set of XMPs can be characterized into subsets based on relative thickness.

To compare the XMP thicknesses in absolute terms, Figure 4.11 plots minor axis vs major axis according to physical size (redshift distance was used to estimate physical size, with a Hubble constant of 70 km/s/Mpc and SDSS-DR7 redshift<sup>4</sup>). The 24 measurements with the greatest error (those above 0.06 in error as shown in Figure 4.9) have been omitted. Indeed we observe smaller galaxies are thicker in relative terms; however, the physical size of their minor axes are smaller compared to the minor axes of larger galaxies. Figure 4.11 shows that the smallest galaxies are the thinnest, less than 1 kpc wide, while the largest galaxies have thicknesses of several kpc.

---

<sup>4</sup>Redshift distance is a reasonable approximation, as only 5 of the XMPs are nearer than 10 Mpc.

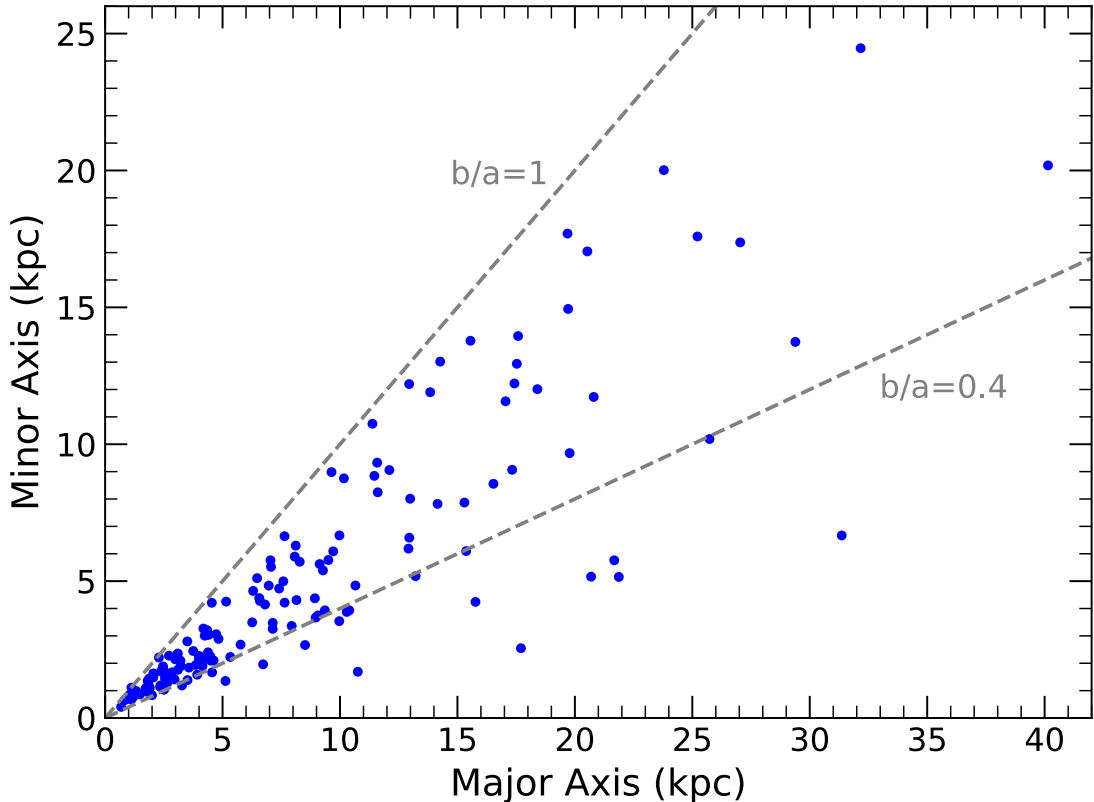


**Figure 4.11:** Minor axis versus major axis in physical size, showing that smaller galaxies tend to be thicker in relative terms, as no XMPs fall beyond the 0.4 axial ratio reference line until 5 kpc, but not in absolute terms. The 24 measurements with the greatest error (above 0.06 in error; see Figure 4.9) are omitted. Physical size was estimated using the SDSS-DR7 redshift and a Hubble constant of 70 km/s/Mpc.

## 4.6 Inferring intrinsic shape

If the axial ratio distribution of the XMPs were predominantly flat and extending all the way to an axial ratio of 1 we could infer that the galaxies are nearly perfect disks. If it peaked at lower axial ratio and continuously dropped with increasing axial ratio we could infer that XMPs are cigar-like in shape (see Figure 2.2). Figure 4.5 does not reflect either of these cases, and thus we can infer that the XMPs are mostly triaxial objects. Given their large relative thickness and probable triaxial intrinsic shape, we can imagine that the XMPs are shaped like compressed rugby balls along the short axis.

In a preliminary effort to quantify the triaxiality of the XMPs, Figure 4.12



shows the observed axial ratio distribution with a theoretical model for randomly oriented ellipsoids with ratio of axes  $1 : 0.7 \pm 0.15 : 0.4 \pm 0.15$ , in which the dispersions follow normal distributions (i.e., the mean value of the second and third axes are 0.7 and 0.4, respectively, with standard deviations of 0.15). The 24 measurements with the greatest error (those above 0.06 in error as shown in Figure 4.9) have been omitted. This model includes mostly triaxial shapes, but it is possible for the second and third axes to be equal at times; thus, some XMPs presumably are very elongated, and a few may even be prolate. The four free parameters were chosen through trial and error, and future work will attempt finding a best fit through a Bayesian approach (e.g., Sánchez-Janssen et al. 2016). Additionally, we know from the previous section that intrinsic shape is not uniform among the XMPs, as relative thickness is observed to increase with decreasing galaxy size. So, fitting the observed axial ratio distribution should consider separating the XMP set based on galaxy size.

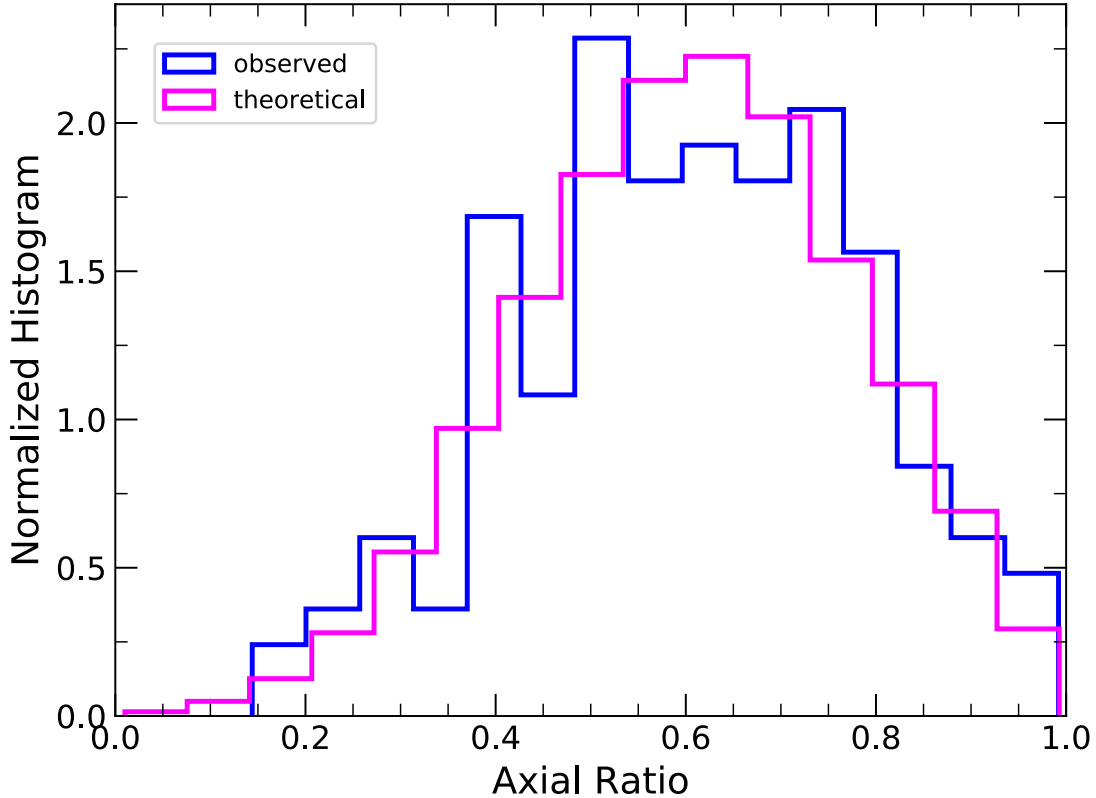


**Figure 4.12:** Normalized observed axial ratio distribution plotted with a theoretical model. The 24 measurements with the greatest error (above 0.06 in error; see Figure 4.9) are omitted. The model was created in the same way as in Section 2.2 but assuming a ratio of axes  $1 : 0.7 \pm 0.15 : 0.4 \pm 0.15$ . The ellipsoids have a distribution of intrinsic shapes in this model, and the dispersions of the two free axes are assumed to follow a normal distribution, with the standard deviation given by the error bars.

The inference of triaxial shapes may also be supported by Figure 4.10, which shows how the surface brightness does not drop to the lowest or highest regions of brightnesses at high axial ratio. If the XMPs were close to perfect disks and assuming almost no internal extinction, then we should observe mean surface brightness to decrease with increasing axial ratio (if viewed face-on, the light is integrated along the short axis; thus, surface brightness is lower). This is not observed. If the XMPs were cigar-like, the mean surface brightness should increase with increasing axial ratio (if viewed end-on, the light is integrated along the longest axis; thus, surface brightness is higher), and the XMPs at highest axial ratio are not highest in surface brightnesses. Figure 4.10 does show there are more high surface brightness XMPs

toward higher axial ratio, and this may be partly due to the starbursts outshining much of the host in many cases in addition to the existence of very elongated shapes. Additional analysis of the surface brightness distribution against axial ratio will be necessary to more confidently draw inferences describing the intrinsic shape(s) of the XMPs.

## 5 Discussion

### 5.1 Why are XMPs thick?

The XMPs are also observed to be thick galaxies, as fall-offs in the axial ratio distribution are observed near 0.4 and 0.5. In comparison, the fall-off for spiral galaxies is  $\sim 0.2$  (e.g., van den Bergh 1988). The reason for their thickness is probably the same reason giving rise to their triaxiality (see item 4 in the following section). The external driving of XMPs from gas accretion will heat them up in their dynamics, causing them to be thicker. Large thickness may also be caused by star formation activity, i.e., internal driving. The kinetic energy released by supernovae and stellar winds are expected to head up the dynamics in a galaxy as well. These forms of external driving and internal driving go hand in hand, as gas accretion is responsible for the starbursts (e.g., Sánchez Almeida et al. 2014).

I observe that the the thickest galaxies (relative to their size) are the smallest ones, and this *downsizing* likely reflects that smaller-mass galaxies evolve more slowly than their more massive counterparts, which are already more relaxed. In other words, smaller galaxies are in earlier stages of their evolution. Also, it is expected that for decreasing galaxy size the ratio of velocity dispersion to rotational velocity increases, which should correlate with increasing relative thickness.

## 5.2 Why are XMPs triaxial?

The results of this work evidence that they XMPs are triaxial objects. The following are possible explanations for triaxiality along with the likelihood that they apply to XMPs.

1. Triaxiality could arise in galaxies experiencing tidal forces. This is unlikely to be the case for XMPs, as this work found that less than 10% of XMPs show signs of interaction (consistent with Filho et al. 2013).
2. Triaxiality could arise due to an intrinsic triaxial gravitational potential, such as in galaxy bulges. This is unlikely to describe XMPs because their baryons are fully dominated by the gas (Filho et al. 2013), and gas has collisions (gas suffers from hydrodynamic forces), and the system quickly tends to relax to an axisymmetric configuration.
3. Triaxiality could be observed because the light distribution of a galaxy is nonaxisymmetric, even though its gravitational potential is axisymmetric. The light distribution of XMPs is nonaxisymmetric, as the galaxies most often have lopsided starbursts that are very bright and outshine much of the host galaxy. However, if the gravitational potential is axisymmetric, then the mass of the starburst(s) most likely would be much smaller than the mass of the host galaxy, and this is not what we observe in XMPs (Elmegreen et al. 2013).
4. Triaxiality could be a transient feature of a galaxy's gravitational potential. XMPs are in the process of formation as they are dwarfs accreting gas, and thus they are not relaxed to an axisymmetric configuration yet. In this scenario, the mass of the starburst(s) most likely would be a significant fraction of the mass of the host galaxy. This is the case for XMPs; thus, this explanation is the proposed most probable one for the triaxiality of the XMPs.

### 5.3 A brief comparison with other studies

Large relative thickness and triaxial intrinsic shape found for the XMPs in this work is consistent with the results of axial ratio studies on irregular galaxies (e.g., van den Bergh 1988), on dwarf irregular galaxies (e.g., Roychowdhury et al. 2013), and on BCDs (e.g., Sung et al. 1998a). Further consistent with this work is that Roychowdhury et al. (2013) also observed relative thickness to increase with decreasing galaxy size, and Sung et al. (1998a) concluded that while most BCDs are triaxial, some may be prolate.

Regarding high redshift, Ravindranath et al. (2006) reported Lyman-break galaxies to be triaxial and suggest lopsided gas accretion in unstable disks is the reason, which is consistent with the proposed reason for triaxiality in this work. They also measured starbursting galaxies at  $z \sim 1.2$  and found an axial ratio distribution consistent with modern-day disks, and they suggest hot-mode accretion, mergers, and bulge formation give rise to a broader axial ratio range. After more robustly quantifying the intrinsic shapes of XMPs, a deeper comparison with the literature will be undertaken.

### 5.4 The environment of XMPs

Another photometric test for how well XMPs support the cold-flow accretion scenario is whether they show signs of on-going mergers, are satellites or have satellites, or show tidal tails, collision rings, or other signs of interaction. In identifying the XMPs suitable for measurement, I found no more than 10% of the original sample of 195 XMPs with possible signs of interaction. This is consistent with previous findings (e.g., Filho et al. 2013).

## 6 Conclusions

1. The axial ratio distribution for a sample of 171 XMPs measured in this work indicates the XMPs are thick, with smaller galaxies being the thickest in proportion to their size. Only 8% of the XMPs have axial ratios less than 0.4, but these galaxies are much larger than the average XMP. No XMPs smaller than 5 kpc in major axis have an axial ratio below 0.4. The sharpest fall-off in the axial ratio distribution is near 0.4, suggesting the most common thickness of XMPs is approximately 0.4 times the major axis. A notable fall-off is also observed near 0.5, and several XMPs have an axial ratio beyond 0.4. Thus, it appears XMPs can be grouped into (at least) three different relative thickness categories. Given that the XMP sample shows different relative thicknesses for different galaxy sizes, fitting the axial ratio distribution should consider separating the XMP sample into subsets based on galaxy size.
2. The axial ratio distribution evidences that the XMPs are notably triaxial, inferred from a largely flat distribution with a dearth of XMPs at high axial ratio. The theoretical distribution for a collection of randomly-oriented ellipsoids with ratio of axes  $1 : 0.7 \pm 0.15 : 0.4 \pm 0.15$  matched against the observed distribution suggests some XMPs are very elongated and possibly prolate due to the overlap in the second and third axes. Triaxiality is also inferred from the observation that surface brightness neither peaks nor drops significantly at axial ratios close to 1. The relation between surface brightness and intrinsic shape for the XMPs deserves further consideration. The relationship is likely complicated by starbursts often outshining the host galaxy to a significant degree, and the role of internal extinction should be considered.
3. Although axial ratio error tends to be small because the XMPs are large in comparison to seeing, smaller XMPs tend to have more inaccurate and less precise axial ratio measurements. Thus, precise fitting of the axial ratio distribution may benefit from seeing-corrected measurements. The SDSS exponen-

tial fit axial ratio is seeing-corrected, but these measurements cannot be used blindly, as the entire region of the XMP hosts occasionally are not identified properly through automatic routines.

4. The dearth of XMPs observed at low axial ratios is not a bias due to seeing, evidenced in this work using a galaxy model to estimate the minimum axial ratios that could be observed. The dearth of XMPs observed at high axial ratio is not due to a surface brightness selection effect, as 99% of the XMPs have brightnesses above the 90% SDSS spectroscopic completeness level.
5. The proposed most likely explanation for the observed triaxiality and thickness of XMPs is that they are galaxies in the process of formation: external driving from gas accretion and internal driving from kinetic energy released by stellar feedback are believed to give rise to a triaxial gravitational potential. It is expected that this is a transient feature, with the galaxy on its way to becoming relaxed.
6. Less than 10% of XMPs show signs of interaction, and this observation supports the cold-flow accretion scenario, predicting that XMPs should appear in low density environments (voids and sheets in cosmological numerical simulations).

## Acknowledgements

I am immensely grateful to my supervisors Jorge and Casiana for the opportunity of this project, for their steadfast commitment to helping me learn, and for the spirit they bring to their work. Thank you also to my defense committee for taking the time to read my work and forcing me to think more deeply about it, which will

help me improve it. I am also very grateful for my friend Javier De Miguel, who generously helped proofread my Spanish.

Funding for SDSS-III has been provided by the Alfred P. Sloan Foundation, the Participating Institutions, the National Science Foundation, and the U.S. Department of Energy Office of Science. The SDSS-III web site is <http://www.sdss3.org/>. SDSS-III is managed by the Astrophysical Research Consortium for the Participating Institutions of the SDSS-III Collaboration including the University of Arizona, the Brazilian Participation Group, Brookhaven National Laboratory, Carnegie Mellon University, University of Florida, the French Participation Group, the German Participation Group, Harvard University, the Instituto de Astrofísica de Canarias, the Michigan State/Notre Dame/JINA Participation Group, Johns Hopkins University, Lawrence Berkeley National Laboratory, Max Planck Institute for Astrophysics, Max Planck Institute for Extraterrestrial Physics, New Mexico State University, New York University, Ohio State University, Pennsylvania State University, University of Portsmouth, Princeton University, the Spanish Participation Group, University of Tokyo, University of Utah, Vanderbilt University, University of Virginia, University of Washington, and Yale University.

## A References

- Alam, S. M. K., & Ryden, B. S. 2002, *ApJ*, 570, 610
- Alam, S., Albareti, F. D., Allende Prieto, C., et al. 2015, *ApJS*, 219, 12
- Amorín, R.O., Aguerri, J.A.L., Muñoz-Tuñón, C., Cairós, L.M. 2009, *A&A*, 501, 75
- Bertin E., Arnouts S., 1996, *A&AS*, 117, 393
- Binggeli, B., & Popescu, C. C. 1995, *A&A*, 298, 63
- Blanton, M. R., Lupton, R. H., Schlegel, D. J., et al. 2005, *ApJ*, 631, 208
- Caon, N., Cairós, L. M., Aguerri, J. A. L., & Muñoz-Tuñón, C. 2005, *ApJS*, 157, 218
- Corbin, M. R., Kim, H., Jansen, R. A., Windhorst, R. A., & Cid Fernandes, R.



2008, ApJ, 675, 194-200

Ceverino D., Dekel A., Mandelker N., et al., 2012, MNRAS, 420, 3490

Ceverino, D., Sánchez Almeida, J., Muñoz Tuñón, C., et al. 2016, MNRAS, 457, 2605

Dekel, A., Birnboim, Y., Engel, G., et al. 2009, Nature, 457, 451

Elmegreen, D. M., Elmegreen, B. G., Rubin, D. S., & Schaffer, M. A. 2005, ApJ, 631, 85

Elmegreen, D.M., Elmegreen, B.G., Sánchez Almeida, J., et al. 2012, ApJ, 750, 95

Elmegreen, B. G., Elmegreen, D. M., Sánchez Almeida, J., et al. 2013, ApJ, 774, 86

Filho, M. E., Winkel, B., Sánchez Almeida, J., et al. 2013, A&A, 558, A18

Hunter, D. A., & Elmegreen, B. G. 2006, ApJS, 162, 49

Izotov, Y. I., Thuan, T. X., & Guseva, N. G. 2012, A&A, 546, A122

Kunth, D., & Östlin, G. 2000, A&ARv, 10, 1

Law, D. R., Steidel, C. C., Shapley, A. E., et al. 2012, ApJ, 745, 85

Morales-Luis, A.B., Sánchez Almeida, J., Aguerri, J.A.L. & Muñoz-Tuñón, C. 2011, ApJ, 743, 77

Papaderos, P., Guseva, N. G., Izotov, Y. I., & Fricke, K. J. 2008, A&A, 491, 113

Putko, J. 2016, Instituto de Astrofísica de Canarias Beca de Verano Memoria

Ravindranath, S., Giavalisco, M., Ferguson, H. C., et al. 2006, ApJ, 652, 963

Reichard, T. A., Heckman, T. M., Rudnick, G., et al. 2009, ApJ, 691, 1005

Sánchez Almeida, J., Muñoz-Tuñón, C., Elmegreen, D. M., Elmegreen, B. G., & Méndez-Abreu, J. 2013, ApJ, 767, 74

Sánchez Almeida, J., Elmegreen, B. G., Muñoz-Tuñón, C., & Elmegreen, D. M. 2014, A&ARv, 22, 71

Sánchez Almeida, J., Pérez-Montero, E., Morales-Luis, A. B., et al. 2016, ApJ, 819, 110

Sánchez Almeida, J., Filho, M. E., Dalla Vecchia, C., & Skillman, E. D. 2017, ApJ, 835, 159

Sánchez-Janssen, R., Ferrarese, L., MacArthur, L. A., et al. 2016, ApJ, 820, 69

- Sérsic J.L., 1968, Atlas de Galaxias Astrales, Cordoba, Argentina: Observatorio Astronomico
- Simonneau, E., Varela, A. M., & Muñoz-Tuñón, C. 1998, Nuovo Cimento B Serie, 113, 927
- Skillman, E.D., Kennicutt, R.C., & Hodge, P.W. 1989, ApJ, 347, 875
- Sung, E.-C., Han, C., Ryden, B. S., Chun, M.-S., & Kim, H.-I. 1998a, ApJ, 499, 140
- Sung, E.-C., Han, C., Ryden, B. S., et al. 1998b, ApJ, 505, 199
- Roychowdhury, S., Chengalur, J. N., Karachentsev, I. D., & Kaisina, E. I. 2013, MNRAS, 436, L104
- van den Bergh, S. 1988, PASP, 100, 344

## **B Color images of omitted XMPs**

Axial ratio was not measured for the following XMPs (see Section 3.1). The index numbers correspond to XMP index number as reported in Sánchez Almeida et al. (2016). Each SDSS mugshot is 50 arcsec across.




























## C Color images of XMPs in order of axial ratio

Axial ratio was measured for the following 171 galaxies, and they are ordered from low to high axial ratio. The index numbers correspond to XMP index number

as reported in Sánchez Almeida et al. (2016). Each SDSS mugshot is 50 arcsec across.



|                            |                           |                            |                           |                            |
|----------------------------|---------------------------|----------------------------|---------------------------|----------------------------|
| 113<br>J122040.33+135320.5 | 87<br>J112237.64+581938.2 | 181<br>J211923.91-004235.3 | 45<br>J093840.27+080811.9 | 70<br>J104801.24+350026.8  |
| 84<br>J112036.72+640115.7  | 88<br>J112244.5+132044.1  | 133<br>J132811.99+021648.8 | 190<br>J223831.1+140027.8 | 160<br>J144555.54+383752.2 |
| 42<br>J092350.09+240827.8  | 91<br>J112824.02+571449.9 | 1<br>J001637.36+003828.7   | 78<br>J110552.92+602228.8 | 155<br>J144027.52+053153.6 |
| 192<br>J232730.54-005114.1 | 95<br>J114506.39+501800.8 | 121<br>J124106.3+343411.7  | 110<br>J121710.2-015425.6 | 196<br>J235424.29+150753.5 |
| 122<br>J124610.69+261501.3 | 36<br>J084236.52+103314.8 | 39<br>J085118.28+471329.3  | 19<br>J030148.95-005258.5 | 135<br>J133549.35+223636   |






















|   |   |   |   |   |
|---|---|---|---|---|
| 59<br>J101655.2+582346.6<br>     | 114<br>J122201.97+632416.4<br>   | 54<br>J100422.75+541432.1<br>    | 124<br>J125432.33+030412.1<br>  | 12<br>J022107.12-002506.1<br>    |
| 68<br>J104213.41+603335.8<br>    | 26<br>J032343.37+003620.8<br>    | 165<br>J152753.09+253837.3<br>   | 157<br>J144330.1+344346.4<br>   | 180<br>J211742.37-001828.9<br>   |
| 62<br>J102355.83+010200.1<br>   | 37<br>J084835.04+304202.5<br>   | 40<br>J090259.98+054823.8<br>   | 161<br>J145729.55+585800.1<br> | 80<br>J111550.51+460638.4<br>   |
| 102<br>J120010.11+104215.7<br> | 137<br>J135154.08+411800.9<br> | 152<br>J142704.78-014348.3<br> | 48<br>J094254.29+340411.6<br> | 103<br>J120122.23+021110.1<br> |
| 50<br>J094705.8+540539.2<br>   | 145<br>J141710.64+104412.5<br> | 116<br>J123048.52+120242.5<br> | 77<br>J110512.67+250352.6<br> | 164<br>J152120.71+395656.9<br> |

|                            |                           |                            |                            |                            |
|----------------------------|---------------------------|----------------------------|----------------------------|----------------------------|
| 109<br>J121547.5+522316.4  | 43<br>J093402.1+551426.4  | 131<br>J132618.64+400404.8 | 46<br>J094053.69+033901.7  | 189<br>J222730.49-093959.8 |
| 76<br>J110241.5+440345.7   | 14<br>J022606.96+000017.9 | 126<br>J125740.66+334135.6 | 176<br>J172201.9+610556.8  | 58<br>J101624.48+375445.8  |
| 129<br>J131117.52+513940.5 | 29<br>J075858.33+283838.2 | 61<br>J102344.97+270639.5  | 195<br>J234038.42-005330.7 | 143<br>J141323.55+130444.3 |
| 146<br>J141851.13+210239.7 | 81<br>J111700.77+215334.8 | 75<br>J105928.33+190914.7  | 69<br>J104700.41+415502.1  | 73<br>J105613.94+120036.5  |
| 92<br>J113341.68+493554.9  | 107<br>J121402.5+534517.9 | 32<br>J081647.76+330330.1  | 175<br>J172000.93+602930.4 | 10<br>J013352.57+134209.5  |

|                            |                            |                            |                            |                            |
|----------------------------|----------------------------|----------------------------|----------------------------|----------------------------|
| 15<br>J024223.56-005817.1  | 183<br>J212657.92-003228   | 82<br>J111834.94+202550.7  | 41<br>J090539.11+534631    | 22<br>J031407.52+005646.2  |
| 151<br>J142524.82+263014.7 | 167<br>J153821.29+465103.6 | 125<br>J125702.61+493641   | 132<br>J132723.27+402204   | 94<br>J114032.08+583832.1  |
| 128<br>J130338.74+003251.4 | 96<br>J114525.83+093053.4  | 184<br>J212732.01+113927.1 | 163<br>J152013.55+400300.9 | 169<br>J155701.58+300527.3 |
| 8<br>J005249.78-084134     | 72<br>J105508.07+511118.5  | 38<br>J085041.84+611618.1  | 16<br>J024428.95+000742    | 33<br>J084029.9+470709.8   |
| 71<br>J105359.98+094953.9  | 21<br>J031345.68+001323.3  | 104<br>J121004.83+015540.2 | 174<br>J170239.91+212008.8 | 144<br>J141356.91+471507   |



|                            |                            |                            |                            |                            |
|----------------------------|----------------------------|----------------------------|----------------------------|----------------------------|
| 27<br>J033128.46+003737.3  | 83<br>J111934.26+513011.9  | 112<br>J122025.85+331431.7 | 141<br>J140802.52+251507.6 | 90<br>J112744.53+081702.5  |
| 6<br>J003741.15+003320     | 11<br>J015759.73+011137.6  | 17<br>J024636.4+001654.8   | 56<br>J101458.65+193219.6  | 57<br>J101547.9+374459.7   |
| 28<br>J033319.17+000311.9  | 34<br>J084045.25+302844    | 5<br>J003630.39+005234.7   | 53<br>J100246.15+165138    | 101<br>J115753.9+563817.5  |
| 118<br>J123518.88+230132.8 | 24<br>J031624.81-010203.6  | 67<br>J103625.04+474153.2  | 191<br>J230209.98+004939.2 | 182<br>J212025.94-005826.3 |
| 23<br>J031426.13-010845.3  | 106<br>J121100.69+524957.4 | 31<br>J080840.85+172856.3  | 139<br>J135953.49+544718.5 | 79<br>J111406.68+104330.1  |

|  |   |  |  |   |
|--|---|--|--|---|
| 179<br>J204827.45-005958.8<br>  | 123<br>J124637.8+521942.2<br>    | 30<br>J080758+341439.2<br>      | 166<br>J153445.45+080924.7<br>   | 63<br>J102754.47+020451.3<br>    |
| 177<br>J173548.74+575734.6<br>  | 65<br>J103026.84+042930.4<br>    | 150<br>J142342.86+225728.7<br>  | 127<br>J130054.61-004152.8<br>   | 173<br>J170022.16+595333.8<br>   |
| 170<br>J160152.51+061233.9<br> | 188<br>J222626.64+134114.4<br>  | 185<br>J212917.31+003933.5<br> | 51<br>J095041.14+104038.1<br>   | 7<br>J004224.81+003315.7<br>    |
| 2<br>J001922.93-002450.4<br>  | 159<br>J144436.55+555705.8<br> | 35<br>J084045.45+320317<br>   | 120<br>J123521.19+273346.6<br> | 168<br>J154357.25+035855.3<br> |
| 99<br>J115441.34+463636.5<br> |   |  |  |   |

## D Additional figures

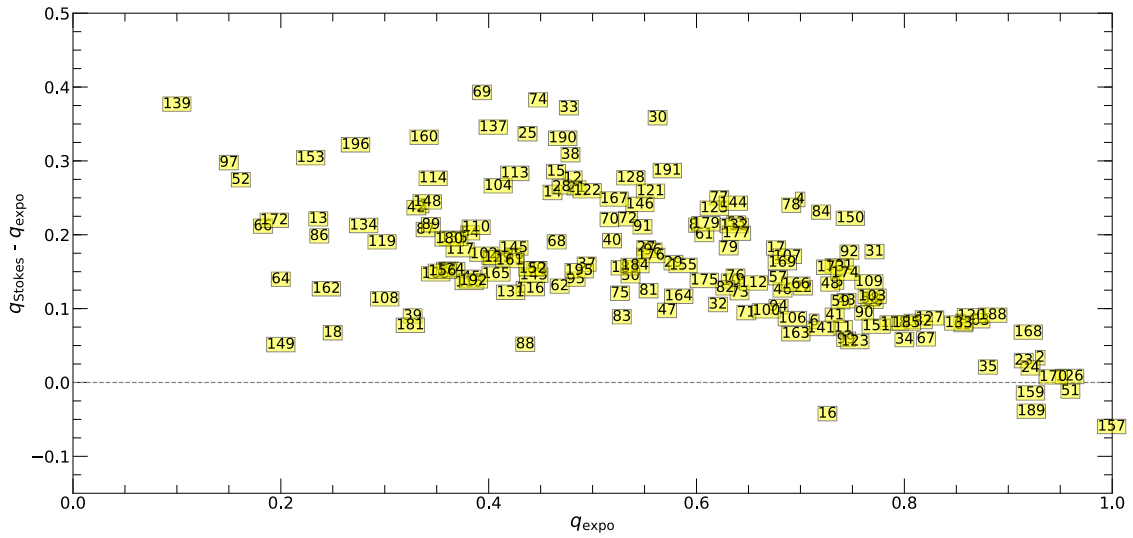


**Figure D.1:** A comparison of two values for axial ratio provided by the SDSS. Axial ratio  $q_{\text{Stokes}}$  is based on flux-weighted second-order moments and is dominated by the central light of the galaxy, while  $q_{\text{expo}}$  is found from an exponential profile fit and is dominated by the outer light (Alam & Ryden 2002).

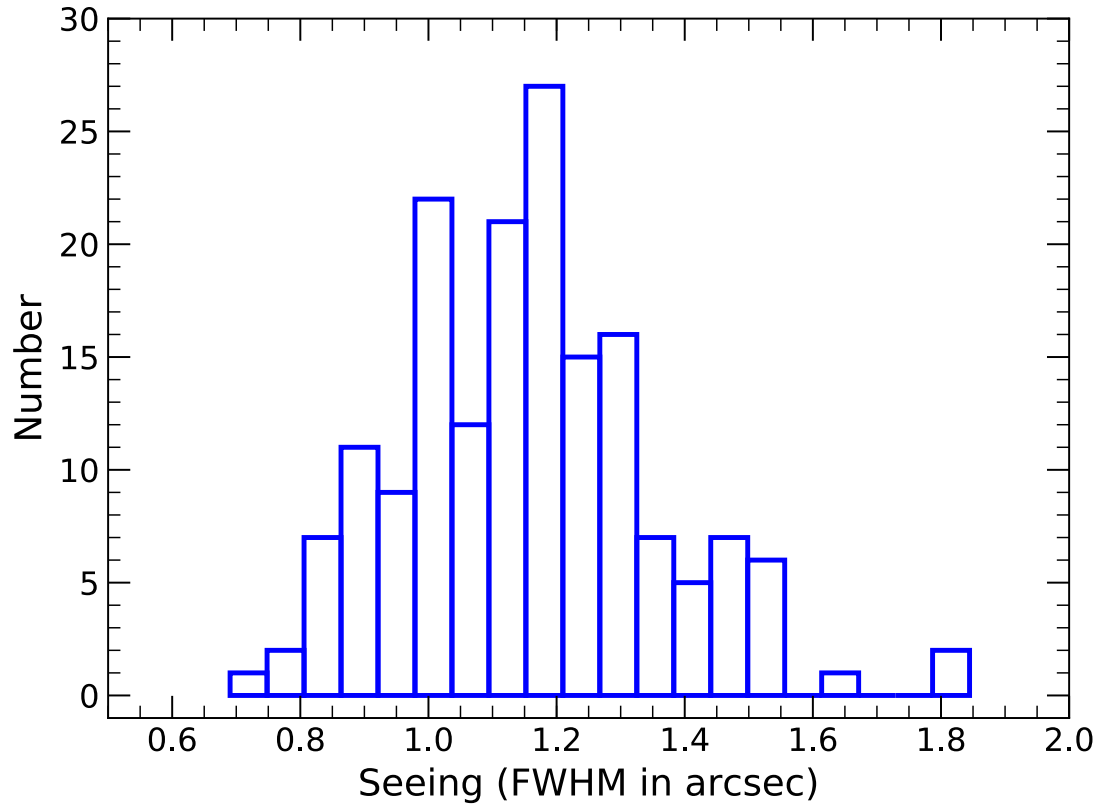


**Figure D.2:** The seeing in the r-band frames containing the XMPs measured in this study. The SDSS measurement “psffwhm” is assumed to represent the seeing. This is the full width at half maximum of the PSF and is provided for each SDSS frame.